Thermally Activated Delayed Fluorescence Emitters with Intramolecular Proton Transfer for High Luminance Solution-Processed Organic Light-Emitting Diodes

Abhishek Kumar Gupta,[†‡] Wenbo Li,[‡] Arvydas Ruseckas,[‡] Cheng Lian,[‡] Cameron L. Carpenter-Warren,[†] David B. Cordes,[†] Alexandra M. Z. Slawin,[†] Denis Jacquemin,[‖] Ifor D. W. Samuel[*‡] and Eli Zysman-Colman[*†]*

[†] Organic Semiconductor Centre, EaStCHEM School of Chemistry, University of St Andrews, Fife, KY16 9ST, UK

[‡] Organic Semiconductor Centre, SUPA. School of Physics and Astronomy, University of St Andrews, North Haugh, St Andrews, Fife, KY16 9SS, UK

[‖] Université de Nantes, CNRS, CEISAM UMR 6230, F-44000 Nantes, France.

KEYWORDS. ESIPT, Proton transfer, TADF, OLEDs, Roll-off efficiency, Luminescence.

ABSTRACT: We report an organic emitter containing a β-triketone electron acceptor core and phenoxazine as the electron donors (**TPXZBM**) for solution-processed organic light-emitting diodes (OLEDs). The resulting molecule is very unusual because it shows both thermally activated delayed fluorescence (TADF) and intramolecular proton transfer. We compare its performance with the previously reported diketone analogue **PXZPDO**. Solution-processed OLEDs of **PXZPDO** and **TPXZBM** show maximum external quantum efficiencies of 20.1% and 12.7%, respectively. The results obtained for the solution-processed **PXZPDO**-based device are as good as the previously reported evaporated device. At a very high luminance of 10,000 cd/m^2 the efficiency of the OLEDs was 10.6% for **PXZPDO** and 4.7% for **TPXZBM**, demonstrating relatively low efficiency roll-off for TADF materials. The low efficiency roll-off was rationalized on the basis of the short delayed lifetimes of 1.35 μs for **PXZPDO** and 1.44 μs for **TPXZBM**. Our results suggest that intramolecular proton transfer may be useful for the design of OLED materials with low efficiency roll-off.

INTRODUCTION:

Organic thermally activated delayed fluorescence (TADF) materials are an attractive class of emitters for organic light-emitting diodes (OLEDs) because they can harvest both singlet and triplet excitons to generate light.[1,2,3,4] Since 2012, numerous TADF emitters have been developed for OLEDs.[5] TADF in typical donor–acceptor (D–A) emitters is facilitated by a small singlet-triplet excited state energy difference, ΔE_{ST}, a consequence of the small exchange integral between weakly overlapping frontier molecular orbitals.[5] The key to realizing TADF is to minimize the ΔE_{ST} so as to maximize the mixing coefficient between these two states, which provides a route for non-emissive triplets to be converted into emissive singlets through thermal activation.[5,6] There

are at present at least six families of TADF emitters, which are donor-acceptor,[5] multi-resonance,[7] spiro-conjugation,[8] exciplex,[9] through space-conjugated,[10] and excited-state intramolecular proton transfer (ESIPT).[11] ESIPT involves the rapid photo-induced tautomerization of a molecule in its electronic excited state and subsequent emission from this second tautomer or both tautomers; in the latter case this would be considered as a dual EISPT-based emitter.[12]

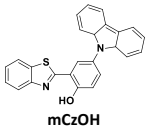

mCzOH
λ_{PL} = 532 nm, ϕ_{PL} = 0.668 in neat powder
λ_{EL} = 546 nm
CIE (0.456, 0.503)
CE_{max} = 2.80 cd A^{-1} in non-doped film

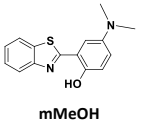

mMeOH
λ_{PL} = 630/535 nm, ϕ_{PL} = 0.056 in neat powder
λ_{EL} = 648 nm
CIE (0.554, 0.382)
CE_{max} = 0.09 cd A^{-1} in non-doped film

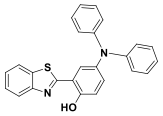

mPhOH
λ_{PL} = 600/502 nm, ϕ_{PL} = 0.375 in neat powder
λ_{EL} = 620 nm
CIE (0.567, 0.374)
CE_{max} = 0.39 cd A^{-1} in non-doped film

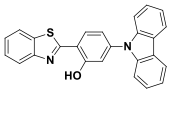

pCzOH
λ_{PL} = 502 nm, ϕ_{PL} = 0.917 in neat powder
λ_{EL} = 500 nm,
CIE (0.267, 0.469)
CE_{max} = 1.10 cd A^{-1} in non-doped film

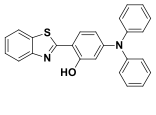

pPhOH
λ_{PL} = 461 nm, ϕ_{PL} = 0.301 in neat powder
λ_{EL} = 460 nm,
CIE (0.157, 0.152)
CE_{max} = 2.30 cd A^{-1} in non-doped film

J. Mater. Chem. **2011**, 21, 3568.

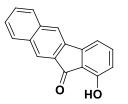

III
λ_{PL} = 450/621 nm, ϕ_{PL} = 0.006/0.2 in CY,
λ_{EL} = 488/590 nm,
EQE_{max} = 0.11%,
CIE (0.26, 0.35) in 5.0 wt% CBP film.
J. Am. Chem. Soc. **2011**, 133, 17738.

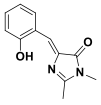

o-HBDI-Z
λ_{PL} = 595 nm, ϕ_{PL} = 0.40 in powder
λ_{EL} = 595 nm,
EQE_{max} = 0.40%,
CIE (0.55, 0.43) in 5.0 wt% CBP film
J. Org. Chem. **2011**, 76, 8189.

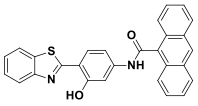

T4AC
λ_{PL} = 552 nm, ϕ_{PL} = 0.781 in THF:water (10:90)
λ_{EL} = 560 nm,
EQE_{max} = 0.46%,
CIE (0.40, 0.49) in non-doped film.
Phys. Chem. Chem. Phys. **2012**, 14, 5289.

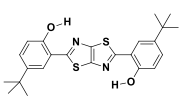

***t*-HTTH**
λ_{PL} = 460 nm,
ϕ_{PL} = 0.2 in neat film
λ_{EL} = 460/550-560 nm,
EQE_{max} = 0.62%,
CIE (0.26, 0.36) in 30% DPEPO film.

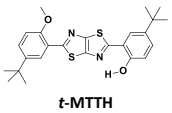

***t*-MTTH**
λ_{PL} = 456 / 572 nm,
ϕ_{PL} = 0.26 in neat film
λ_{EL} = 460/550-560 nm,
EQE_{max} = 1.70%,
CIE (0.29, 0.33) in 30% TCB film

Chem. Mater. **2016**, 28, 8815−8824

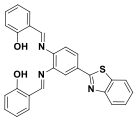

BTS
λ_{PL} = 547/480 nm, ϕ_{PL} = 0.004 in DCM
λ_{EL} = 525/415 nm, CE_{max} = ~8 mcd A^{-1}
CIE (0.31, 0.40) in 1.0 wt% PVK film
Phys. Chem. Chem. Phys. **2019**, 21, 1172.

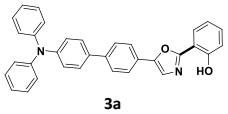

3a
λ_{PL} = 444 nm, ϕ_{PL} = 0.41, **ΔE_{ST} = 0.789 eV**
in 5.0 wt% PS film
λ_{EL} = 443 nm, EQE_{max} = 7.1%,
CIE (0.15, 0.08) in 13.0 wt% CBZ_2-F_1 film
Adv. Funct. Mater. **2017**, 27, 1605245.

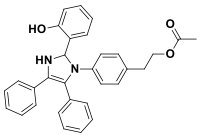

HPI-Ac
λ_{PL} = 465 nm, ϕ_{PL} = 0.22 in DCM
ΔE_{ST} = 0.078 eV
J. Phys. Chem. A **2007**, 111, 9649.

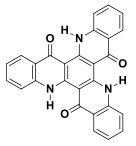

TQB
λ_{PL} = 516 nm, ϕ_{PL} = 0.55, **ΔE_{ST} < 0.2 eV**,
in 10. wt% CzSi film
λ_{EL} = 518 nm, EQE_{max} = 14.2%
in 10.0 wt% CzSi film
ACS Cent. Sci. **2017**, 3, 769.

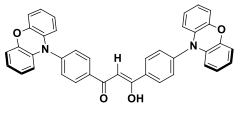

PXZPDO
λ_{PL} = 552 nm, ϕ_{PL} = 0.68, **ΔE_{ST} = 0.04 eV**
in 1.0 wt% CBP film
λ_{EL} = 560 nm, EQE_{max} = 18.8 %,
CIE (0.44, 0.53) in 1.0 wt% CBP film
J. Am. Chem. Soc. **2018**, 140, 8877.

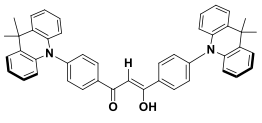

DMACPDO
λ_{PL} = 524 nm, ϕ_{PL} = 0.86, **ΔE_{ST} = 0.11 eV**
in 6.0 wt% CBP film
λ_{EL} = 536 nm, EQE_{max} = 23.9 %,
CIE (0.36, 0.57) in 6.0 wt% CBP film
J. Am. Chem. Soc. **2018**, 140, 8877.

Chart 1. Chemical structures and related photophysics and OLEDs of reported fluorescent ESIPT (black) and ESIPT-based TADF emitters (blue).

ESIPT luminescence is thus characterized by large changes in the Stokes shift and an emission that can be tunable by the local environment.[12,13,14] A potential consequence of ESIPT is that the electron density distribution of the frontier molecular orbitals can change significantly between the two tautomeric forms, leading to changes in $\Delta E_{ST,}$ which will then affect the efficiency of TADF. Because of these unique photophysical properties, ESIPT molecules are attractive for fluorescence sensing, bioimaging, NIR emitters, UV absorbers as well as for lighting materials.[12,13,14,15] Additionally, a small number of reports exist that employ ESIPT-based fluorophores as emitters in OLEDs (Chart **1**);[11,16,17,18,19,20,21,22,23,24] however, the performance of these devices is poor, in part due to the inefficient harvesting of excitons. The first report of a molecule (**HPI-Ac**) exhibiting both ESIPT and TADF dates back to 2007; however, no OLEDs were fabricated.[23] Recently, Mamada *et al*.[11] reported the first use of a TADF ESIPT emitter, triquolonobenzene (**TQB**), in an OLED. The OLED achieved a maximum external quantum efficiency, EQE_{max}, of 14%. Wu *et al*. reported TADF emitters with a proton transfer active site that they claimed was ESIPT based on a molecular design containing a β-diketone acceptor core and either phenoxazine (PXZ) or 9,9-dimethyl-9,10-dihydroacridine (DMAC) as the donor moieties (**PXZPDO** and **DMACPDO**).[24] The OLEDs employing these two emitters achieved EQE_{max} of 18.8% and 23.3%, respectively in vacuum-evaporated devices. Inspired by this work, we designed a new TADF emitter, tris(4-(10H-phenoxazin-10-yl)benzoyl)methane (**TPXZBM**) that incorporates a β-triketone acceptor, which contains a stronger acceptor moiety and so can shift the emission to the red in comparison to **PXZPDO**. Additionally, the β-triketone contains a more acidic methine proton, allowing for the co-existence of two tautomers, and additionally allowing

rapid proton transfer between two forms as in **PXZPDO**. Indeed, we hypothesized that the enol tautomer in **TPXZBM**, in which ESIPT should be possible, would be significantly more stabilized in the ground state than the ESIPT-locked β-triketone (Scheme **1**). Indeed, the keto-enol tautomerization behavior in β-triketone-containing compounds has been previously reported[25,26] and the enol tautomer was observed in solution.[26] We cross compare the optoelectronic properties and OLED device performance of this compound with both the reference **PXZPDO** emitter and the β-tetraketone control emitter, bis-(4-bromobenzoyl)bis-(4-(10*H*-phenoxazin-10-yl)benzoyl)methane (**BPXZBM**), which does not contain an enolizable proton and so does exist as one tautomer only (Scheme **2**). We demonstrate that **TPXZBM** shows both ESIPT and TADF, with the enol tautomer dominant in the excited state, resulting in a ΔE_{ST} of 20 meV and a short delayed fluorescence lifetime, τ_d, of 1.44 μs in 4,4′-bis(*N*-carbazolyl)-1,1′-biphenyl (CBP) host. The solution-processed OLED devices showed EQE_{max} values of 20.1%, 12.7% and 7.0% for **PZXPDO**, **TPXZBM** and **BPXZBM**, respectively. Importantly, the EQEs of **PXZPDO** and **TPXZBM** at 10,000 cd/m^2 reached 10.6% and 4.7%, respectively. This is, to the best of our knowledge, the first report of solution-processed TADF OLEDs that also show intramolecular proton transfer. Vacuum evaporation is widely and successfully used as a fabrication technique, but solution-processing offers the prospect of simpler deposition and patterning, simpler device structures and more efficient utilization of materials.[27,28]

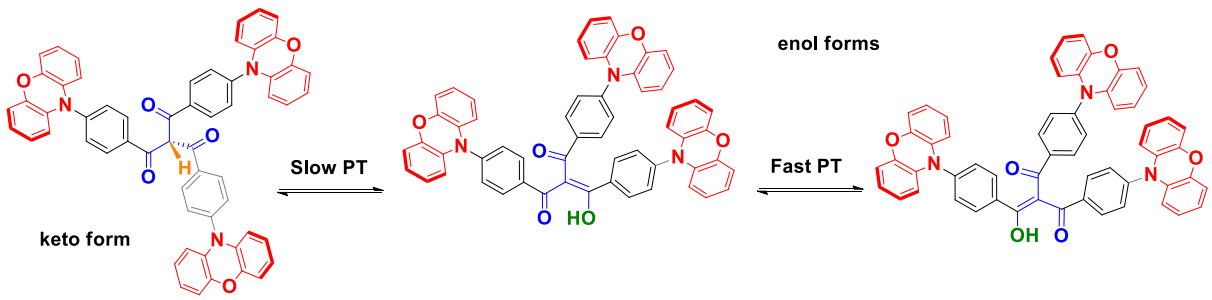

Scheme 1. β-triketone tautomers of **TPXZBM**.

RESULTS AND DISCUSSION:

Synthesis and structure characterization.

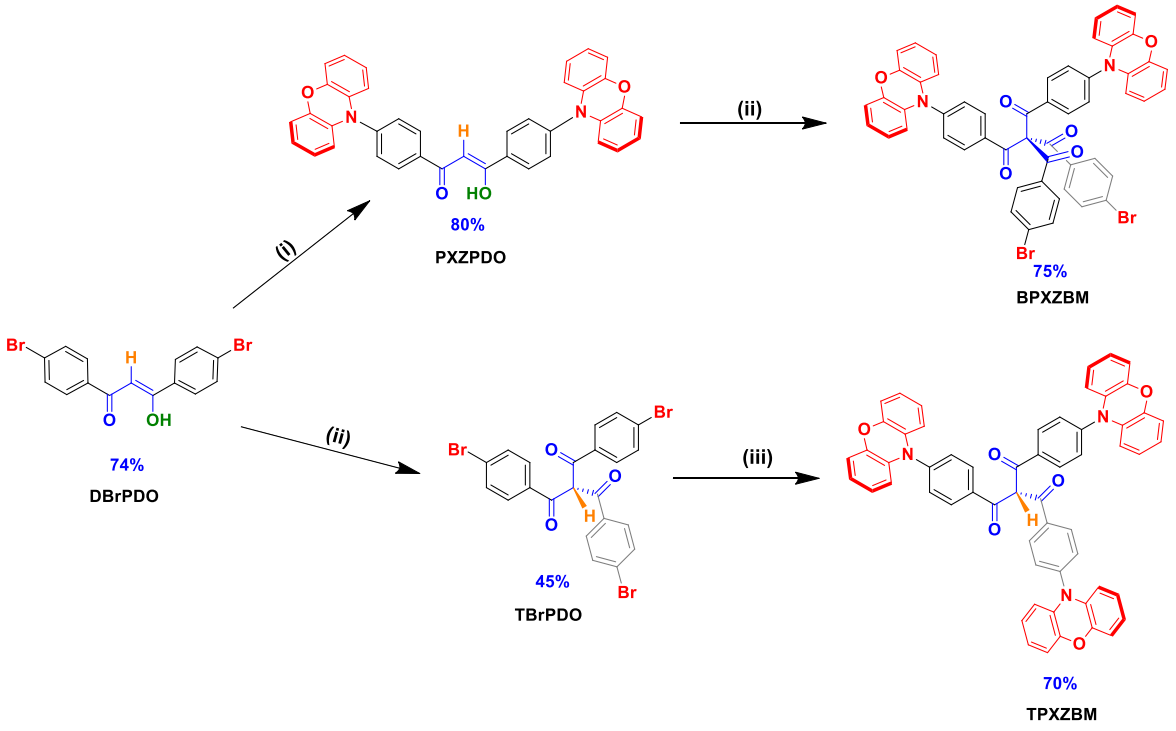

Scheme 2. Synthetic scheme. i) 10-*H*-phenoxazine, $[Pd(OAc)_2]$, $[(^tBu)_3PH]BF_4$, NaO^tBu; ii) NaH, 4-Br-benzoylchloride; iii) 10-*H*-phenoxazine, $[Pd(OAc)_2]$, $[(^tBu)_3PH]BF_4$, Cs_2CO_3.

PXZPDO was synthesized in 80% yield following the previously reported procedure (Scheme **2**).[24] Adapting a literature protocol for the synthesis of β-triketones,[29] the tribromo-substituted β-triketone intermediate, **TBrPDO**, was obtained in moderate yield. The emitter **TPXZBM** was obtained in 70% yield through the palladium-catalysed Buchwald–Hartwig cross coupling between **TBrPDO** and PXZ.[30] The control emitter **BPXZBM** was obtained in 75% yield following deprotonation with NaH and double acylation of the corresponding β-diketonate of **PXZPDO**. The

identity and purity of the three emitters were determined by a combination of ^{1}H and ^{13}C NMR spectroscopy, high-resolution mass spectrometry (HRMS), melting point determination and elemental analysis (see Experimental section and Supporting Information, Figure **S1-S24**).

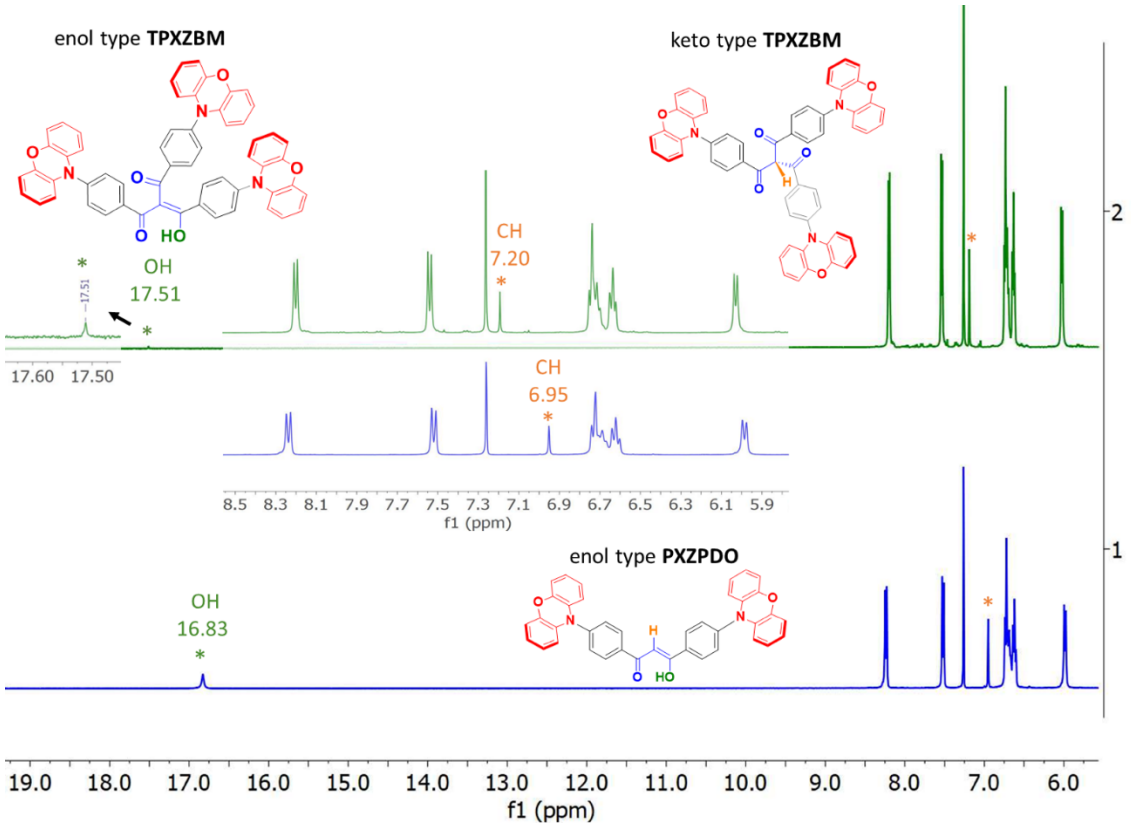

Figure 1. ^{1}H NMR spectrum of **PXZPDO** and **TPXZBM** in $CDCl_3$.

The ^{1}H NMR spectrum in $CDCl_3$ of **PXZPDO** reveals that only the enol tautomer is present (Figure **1**), similarly to that reported in the literature.[24] By contrast, the ^{1}H NMR spectrum of **TPXZBM** shows that the keto tautomer is the major form in a 4:1 ratio with the enol form, a ratio calculated from integral ratio of the ketonic methine proton and enolic hydroxy proton (Figure **1**). There is therefore a slow (i.e., slower than the NMR timescale) equilibrium between the two tautomers in **TPXZBM**. The enol OH resonance shifts from 16.83 ppm in **PXZPDO** to 17.51 ppm in **TPXZBM** while the methine proton also shifts downfield from 6.95 ppm to 7.20 ppm, a reflection of the more

acidic nature of both protons in **TPXZBM** and suggesting the existence of strong intramolecular H-bond (IHB) in the enol tautomer of **TPXZBM**.[25,26,31] We next explored the impact of solvent polarity on the strength of the IHB and the tautomer ratio of **TPXZBM** (Figures **S13-S18**). Regardless of solvent, the major tautomer of **TPXZBM** is the keto form. In non-polar solvents such as toluene-d_8 and CD_2Cl_2, the keto/enol tautomeric ratios are 2.7:1 and 3.7:1. In THF-d_8 and acetone-d_6 the keto/enol ratios are 1:0.9 and 1:0.8, respectively. In DMSO-d_6, the enol OH resonance was not observed, likely due to proton exchange between residual water in DMSO-d_6 and the enol form of **TPXZBM**. The keto/enol tautomeric ratios are approx. 3.2:1 in DMSO-d_6 calculated from the integral ratio of the ketonic phenyl resonances and enolic phenyl resonances. In CD_3OD only the keto form of **TPXZBM** is present; however, the methine resonance was not observed due to the acidic nature of this proton, likely due to proton exchange with CD_3OD (Figure **S18**). The methine resonance of the keto-form of **TPXZBM** shifted progressively downfield with increasing solvent polarity (Figures **S13-S17**), indicative of the more acidic nature of methine proton. By contrast, the enol OH resonance shifted upfield with increasing solvent polarity (see Figures **1**, **S13**-**S17** and Table **S1**,). We next probed the effect of temperature on the ^{1}H NMR spectra of **TPXZBM** and **PXZPDO** in $CDCl_3$. Upon cooling the sample of **TPXZBM** to -40 ^{o}C, the chemical shift of the ketonic methine proton of **TPXZBM** shifts downfield by 0.23 ppm (Figure **S19**). By contrast, the chemical shift changes of the corresponding vinyl proton in **PXZPDO** is negligible ($\Delta\delta$ = 0.04 ppm), Figure **S20**, whereas the chemical shift of the enol OH resonances in both molecules shifted to a similar extent ($\Delta\delta \approx 0.39$ ppm), which favours proton transfer form (i.e., weakening of the O–H bond and strengthening the adjacent H···O hydrogen bonding).[32,33] Although the ratio of the keto/enol tautomers vary, these results all support the

presence of the enol tautomer and intramolecular H-bond in **TPXZBM** over a wide range of solvent polarities.

Single crystal X-ray diffraction of **TPXZBM** revealed that only the keto tautomer exists in the crystal. The asymmetric unit consists of one molecule of **TPXZBM** (Figure **2** and Figure **S25**, Table **S2**). The dihedral angles between the bridging phenyl rings and the mean planes of the PXZ donor moieties are 65.95(15)°, 64.49(13)° and 75.98(15)°, indicating a highly twisted structure. A similar set of dihedral angles between PXZ units and bridging phenyl groups was also observed in **PXZPDO**.[24] All three carbonyl groups **TPXZBM** are oriented in the same direction leading to a propeller-like overall shape, making the molecule helically chiral.

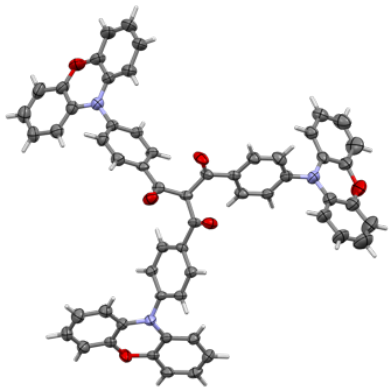

Figure 2. Thermal ellipsoid plot of the crystal structure of **TBXZBM**. Ellipsoids are plotted at the 50% probability level and hydrogens are omitted for clarity.

Theoretical calculations on the different tautomers.

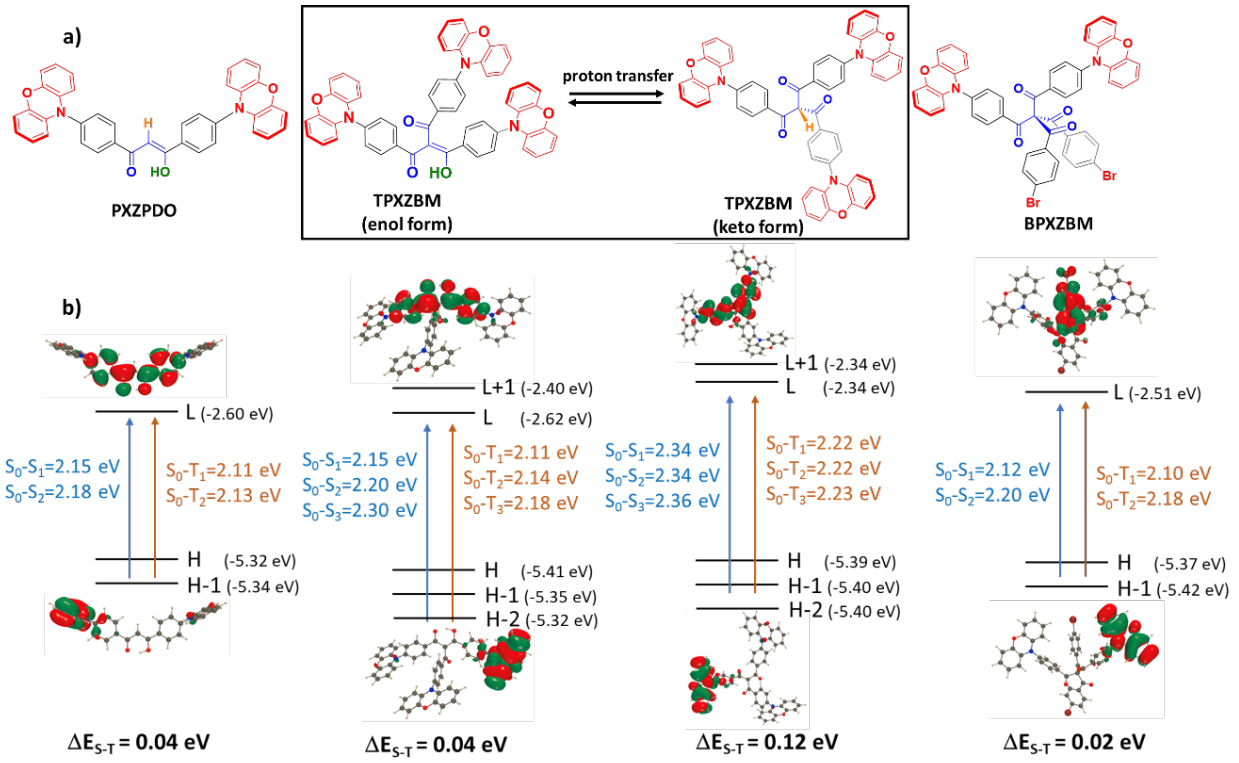

Figure 3. (a) Molecular structures of **PZXPDO, TPXZBM** (enol and keto tautomers) and **BPXZBM**; (b) Highest occupied molecular orbital (HOMO) and lowest unoccupied molecular orbital (LUMO) distributions, and theoretical calculated frontier MO energy levels of all compounds, together with the transition energies for the relevant lowest S and T states, as given by TD-DFT. The displayed HOMO and LUMO electron density distributions are representative of the other largely pseudo-degenerate occupied and unoccupied molecular orbitals.

To determine the dominant forms in the ground (S_0) and lowest excited (S_1 and T_1) states, density functional theory (DFT) and time-dependent DFT (TD-DFT) calculations were performed (see Experimental Section for the computational details). The enol tautomer of **PXZPDO**, presenting

an intramolecular hydrogen bond, is more stable than its keto counterpart by 3.5 kcal.mol^{-1} in the S_0 state, and is therefore the only form at room temperature, consistent with the NMR measurements as well as with a previous report.[24] In **TPXZBM** the β-triketone group can exist as keto and enol form, the latter being an "enol diketone form of a triketone". Therefore, the tautomeric equilibrium can give two different structures, **TPXZBM**-enol form and **TPXZBM**-keto form as shown in Figure **3a**. Consistent with the crystal structure, the keto tautomer of **TPXZBM** shows a non-planar conformation, with all carbonyl groups aligned in a helical fashion but on the opposite face to the methine hydrogen (CH). The structure of enol form is significantly different, implying that any change in the tautomeric equilibrium will require a major geometrical rearrangement, which is likely to be slow, as confirmed by the presence of distinct resonances in the NMR for both tautomers. The DFT calculations suggest that the keto tautomer of **TPXZBM** is slightly more stable than the enol form in the ground state by 0.3 kcal.mol^{-1}. Although such value falls within the DFT error bar, it clearly indicates that the enol and keto tautomers have very much alike energies and should coexist at room temperature. This theoretical result is also consistent with the ^{1}H NMR results, which show the presence of both forms but a more abundant keto-type **TPXZBM**. The reference molecule tetraketone (**BPXZBM)** exhibited only a ketone-type form because the disubstitution of the β-diketone core of **PXZPDO** eliminates the possibility of an enol-type tautomer. An aspect that we believe was partly overlooked previously,[24] is the ground-state equilibrium between the two equivalent enol-type tautomers. Indeed, in both **PXZPDO** and **TPXZBM**-enol, rapid proton transfer can occur as shown in the right-hand side of Scheme **1**, resulting in an COH/C=O equilibrium. In both **PXZPDO** and **TPXZBM**-enol, the two tautomers created in this way are nearly equivalent due to the pseudo-symmetry. DFT calculations indicate that the energy required for interconversion of the two enol tautomers is 1.6 kcal.mol^{-1} for

PXZPDO and 1.1 kcal.mol^{-1} for **TPXZBM**. This is a very small barrier that will be further reduced by vibrational corrections, leading to easy and rapid interconversion of the two tautomers. In other words, the "ESIPT" mentioned in the previous study,[24] is in fact a proton transfer already occurring in the ground state and not a specific signature of the excited state (*vide infra*).

The lowest singlet state, S_1, reached after photon absorption, has also been investigated computationally, again with geometries optimized for the various tautomers. For **PXZPDO**, the enol form remains more stable than its keto counterpart by 4.3 kcal.mol^{-1}. There is a slight elongation of the OH bond length, and the proton transfer remains barrierless as in S_0 (when vibrational corrections are accounted for). This implies that the proton transfer is both very fast (ca. ps timescale), and that the proton is constantly transferring from one oxygen atom to the other. In this sense, **PXZPDO** (and likely **DMACPDO**) should be distinguished from the other compounds of Chart **1**. Indeed, in all other systems, the proton-donating and accepting groups do differ significantly, so that a tautomeric form that is not present in S_0 becomes accessible after photon absorption, as in most "classical" ESIPT systems. By contrast, for **PXZPDO** there is a constant proton transfer between two equivalent tautomers in both electronic states. In the calculated S_1 minimum of **TPXZBM**, we found that the enol tautomer is now significantly favoured by 2.6 kcal.mol^{-1} as compared to the keto; meaning there is now a significant thermodynamic driving force to produce the enol form, and the photon absorption produces a change of the most stable tautomer, consistent with a "classical" ESIPT system. As in all previous cases, the rapid proton exchange between the two oxygen atoms in **TPXZBM**-enol is found to be barrierless.

The lowest energy vertical transitions are displayed for all systems in Figure **3b**. For **PXZPDO**, we found as expected that the HOMO and HOMO-1 are nearly degenerate and located on the

phenoxazine donors groups, whereas the LUMO is centred on the β-diketone unit. Therefore, the lowest energy transition has a strong CT character (Figure **S26**). Furthermore, the orthogonality of the phenoxazine donors with respect to the bridging phenylene groups leads to negligible orbital overlap, and hence a minute ΔE_{ST}. Indeed, as can be seen, the S_0-S_1, S_0-S_2, S_0-T_1, and S_0-T_2 transitions, that all involve (mixed) HOMO to LUMO and HOMO-1 to LUMO electron promotions, are all nearly degenerate with a ΔE_{ST} of only 0.04 eV. For **TPXZBM**-enol form, the trends and energy levels are extremely similar to those of **PXZPDO** (ΔE_{ST} = 0.04 eV), but more low-lying transitions (involving from HOMO-2 to LUMO+1) appear due to the additional donating group (see MOs in Table **S3**). The contrast is significant with **TPXZBM**-keto, in which the singlet-triplet gap is now significantly larger (0.12 eV), although the singlet and triplet excitations are themselves degenerate due to the pseudo D_3 symmetry (see Table **S3** for all MOs). As can be seen in Figure **3b** the LUMO of **TPXZBM**-enol is significantly deeper (-2.60 eV) than in **TPXZBM**-keto (-2.34 eV), a result of increased conjugation in this form. In the case of the reference molecule **BPXZBM**, the HOMO energy level is -5.37 eV and located on the phenoxazine unit like in other molecules while the LUMO is mainly located on the 4-bromobenzoyl unit, although the ΔE_{ST} remains very small in this compound. In short, these calculations suggest that enol-type **TPXZBM** should have very similar behavior to **PXZPDO**. Finally, in Table **S4**, we provide the spin density of the lowest triplet excited states for all compounds, and this similarity is also apparent.

Electrochemistry.

Cyclic voltammetry (CV) and differential pulse voltammetry (DPV) in dichloromethane (DCM) with tetra-*n*-butylammonium hexafluorophosphate ($TBAPF_6$) as the supporting electrolyte were

used to determine the redox potentials of **PXZPDO**, **TPXZBM** and **BPXZBM**. The resulting voltammograms are shown in Figure **S27** and the data are summarized in Table **1**. Given that the keto/enol equilibrium is sensitive to the polarity of the medium, it is likely that the speciation within the electrochemical cell for **TPXZBM** differs from that observed by ^{1}H NMR in DCM. All three emitters possess similar quasi-reversible oxidation potentials around 0.83 V vs SCE, which are assigned to the oxidation of the phenoxazine donor moieties. The estimated HOMO levels are -5.13 eV, -5.17 eV and -5.18 eV for **PXZPDO**, **TPXZBM** and **BPXZBM**, respectively, which are in line with the values and trends calculated from DFT. **PXZPDO** shows a quasi-reversible reduction wave at -1.32 V; it is unclear whether this is associated with the reduction of the β-diketone acceptor. In the prior report for **PXZPDO** only the oxidation potential was documented and the estimated HOMO and LUMO levels are -5.14 eV and -2.73 eV, respectively.[24] The reduction of **BPXZBM** is quasi-reversible and is shifted significantly anodically to -1.13 V compared to that of **PXZPDO**. By contrast, the reduction of **TPXZBM** is irreversible and shifted cathodically to -1.42 V; the reduction shows significantly weaker current intensity in comparison to the oxidation potential and we also observed that current density slightly increased with increasing the scan rate from 100 mV/s to 500 mV/s (Figure **S28**). The LUMO energy levels estimated from the difference between HOMO energy and the optical gap (ΔE_g) of **PXZPDO**, **TPXZBM** and **BPXZBM** are -2.70 eV, -2.70 eV and -2.78 eV, respectively (Table **1**).

Table 1. Electrochemical, HOMO-LUMO and ΔE_{ST} of **PXZPDO**, **TPXZBM** and **BPXZBM**.

Emitters	E_g[a], / eV	E_{ox}[b] / V	E_{red}[b]/ V	HOMO[c] /eV	LUMO[d] / eV	E_S/E_T[e], / eV	ΔE_{ST}[f] / eV
PXZPDO	2.43	0.79	−1.32	−5.13	−2.70	2.45/ 2.41	0.04
TPXZBM	2.47	0.83	−1.42	−5.17	−2.70	2.40/ 2.38	0.02
BPXZBM	2.40	0.84	−1.13	−5.18	−2.78	2.380/ 2.385	0.005

[a] Obtained from the intersection of the normalised absorption and emission spectra in PhMe. [b] E_{ox} and E_{red} are anodic and cathodic peak potentials, respectively, obtained from DPV using F_c/F_c^+ as the internal reference (0.46 V vs. SCE) in DCM with 0.1 M [nBu$_4$N]PF$_6$ as the supporting electrolyte.[34] [c] The HOMO energies were determined using $E_{HOMO} = -(E_{ox} +$

4.8),[35] where E_{ox} is anodic peak potential obtained from DPV relative to F_c/F_c^+. [d] $E_{LUMO} = |E_{HOMO} - E_g|$. [e] Obtained from onset of prompt fluorescence (time window: 1 ns – 100 ns) and phosphorescence spectra (time window: 1 ms – 10 ms) of 1 wt% samples doped in CBP at 77 K. [f] $\Delta E_{ST} = E_S - E_T$.

Table 2. Photophysical properties of **PXZPDO, TPXZBM** and **BPXZBM.**

Emitters	λ_{abs} / nm, (ε /×10^{-4}M^{-1}cm^{-1})	λ_{PL} / nm	τ_p / ns	τ_d / μs	R_p/R_d[d]	ϕ_{PL} / %
		In toluene[a]				
PXZPDO	335 (3.6), 440 (0.65)	604	7.5	0.62	0.82/0.18	18[b]
TPXZBM	324 (3.8), 440 (0.66)	650	6.9	0.44	0.80/0.20	1[b]
BPXZBM	321 (1.6), 438 (0.31)	626	6.3	0.43	0.88/0.12	0.2[b]
		1 wt% doped in polymethylmethacrylate (PMMA)[c]				
PXZPDO	331, 440	572	15.5	1.07	0.63/0.37	35
TPXZBM	320, 440	582	14.9	1.01	0.87/0.13	13
BPXZBM	321, 438	593	16.2	0.71	0.81/0.19	10
		1 wt% doped in CBP[c]				
PXZPDO	331, 460	568	16.8	1.35	0.68/0.32	58
TPXZBM	331, 477	578	14.3	1.44	0.85/0.15	30
BPXZBM	332, 442	592	21.8	1.01	0.87/0.13	17

[a] At 298 K. [b] $[Ru(bpy)_3]Cl_2$ in water was used as the reference, (ϕ_{PL} = 2.8 % in air, λ_{exc} = 448 nm).[36,37] [b] Values quoted are in degassed solutions, which were prepared by three freeze-pump-thaw cycles. [c] Thin films were prepared by spin-coating 1 wt% doped samples in PMMA and CBP. Steady-state and time-resolved emission spectra were recorded at 298 K under an O_2-free atmosphere (λ_{exc} = 340 nm for steady-state and λ_{exc} = 378nm for time-resolved emission). Photoluminescence quantum yields of thin films were determined using an integrating sphere (λ_{exc} = 300 nm for molecules dispersed in CBP and λ_{exc} = 420 nm for molecules dispersed in PMMA) under N_2 atmosphere at 298 K. [d] The weighting factors for prompt and delayed fluorescence.

Photophysical properties in solution

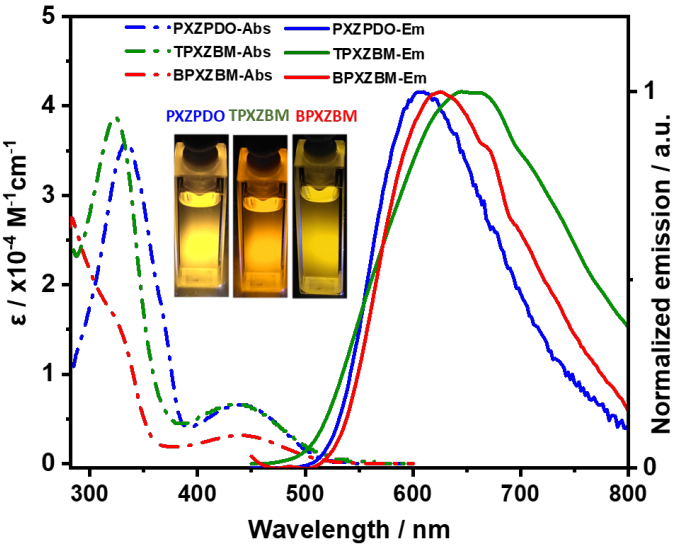

Figure 4. Molar absorptivity and photoluminescence spectra of **PXZPDO, TPXZBM** and **BPXZBM** in toluene at 298 K (λ_{exc} = 340 nm). Inset: Photos of photoexcited solutions in toluene.

All three molecules show similar absorption spectra in dilute toluene, with two main absorption bands (Figure **4**, Table **2**). The absorption spectrum for **PXZPDO** matches well with the literature.[24] The stronger of the two main bands, at around 324 nm, corresponds to a locally excited (LE) π-π* transition on phenoxazine.[38] This band is more intense for **TPXZBM** compared to **PXZPDO** (3.8×10^{-4} $M^{-1}cm^{-1}$ *vs* 3.6×10^{-4} $M^{-1}cm^{-1}$) whilst the corresponding band in **BPXZBM** is much less intense (1.6×10^{-4} $M^{-1}cm^{-1}$). The longer wavelength absorption band at 440 nm is assigned to an intramolecular charge transfer (ICT) transition from phenoxazine to the β-diketone, β-triketone or β-tetraketone acceptor cores of **PXZPDO**, **TPXZBM** and **BPXZBM**, respectively. This assignment is consistent with the TD-DFT analysis (see Figure **S26**). The very similar energies of these ICT bands indicate that there is no significant electronic communication between the ketone units in these compounds. **PXZPDO** and **TPXZBM** show very similar molar absorptivity of 6.5×10^{-3} $M^{-1}cm^{-1}$, which is about twice as large than in **BPXZBM** ($\varepsilon = 3.1\times10^{-3}$ $M^{-1}cm^{-1}$). TD-DFT also foresees smaller oscillator strengths for **BPXZBM** than for the two other molecules, consistent with this experimental outcome.

The photoluminescence (PL) spectra of all three emitters in toluene are shown in Figure **4**. The PL maximum of **TPXZBM** occurs at 650 nm and is red-shifted relative to **PXZPDO** (λ_{PL} = 604 nm) and **BPXZBM** (λ_{PL} = 626 nm), a general position reproduced by the calculations (Table **S4**). The full width at half maximum (FWHM) is wider in **TPXZBM** (0.59 eV vs 0.43 eV in **PXZPDO** and

0.47 eV in **BPXZBM**). The Stokes shifts are 7343 cm^{-1} for **TPXZBM**, 6171 cm^{-1} for **PXZPDO** and 6857 cm^{-1} for **BPXZBM**.

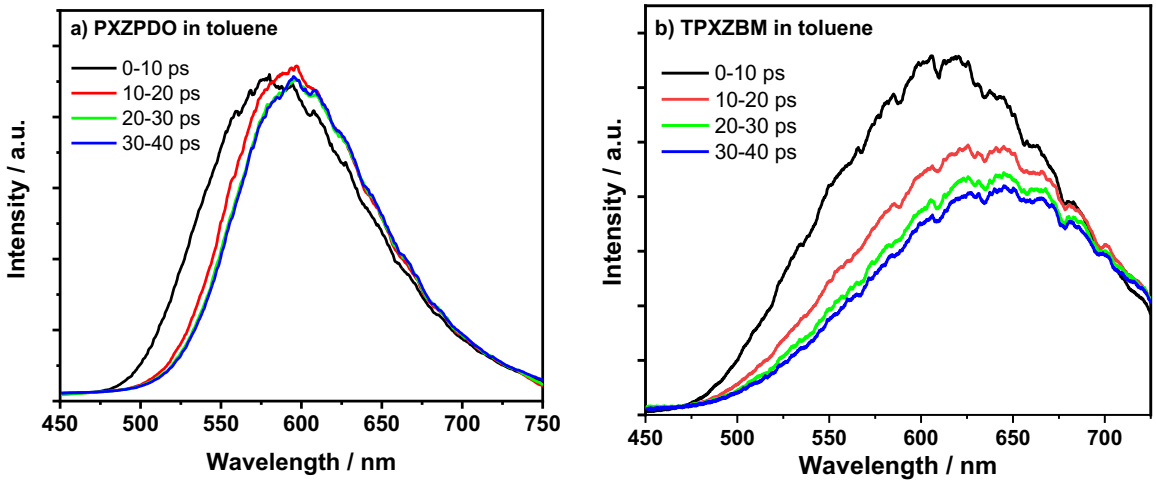

Figure 5. Time-resolved fluorescence spectra of (a) **PXZPDO**; and (b) **TPXZBM** in toluene. λ_{exc} = 400 nm.

In order to obtain a clearer picture of the excited state dynamics we measured time-resolved fluorescence spectra of these emitters in toluene (Figure **5**). The fluorescence spectrum of **TPXZBM** measured in the 10-20 ps time window shows a maximum at ~630 nm, which is red-shifted with respect to the spectrum acquired in the 0-10 ps window (λ_{PL} ~610 nm). The emission maximum red-shifts to ~640 nm after a ~30 ps delay and then resembles the time-integrated PL spectrum (Figure **4**). The peak fluorescence intensity of the 30-40 ps spectrum is reduced by ~35% as compared to the 0-10 ps spectrum, which is followed by a much slower decay. **PXZPDO** shows a significantly smaller red-shift of the 10-20 ps and 20-40 ps spectra (λ_{PL} ~590 nm) relative to the 0-10 ps spectrum (λ_{PL} ~580 nm) but no decay in intensity on this time scale. The small dynamic red-shift in **PXZPDO** can be explained by solvation of the excited emitter. The intensity decay observed for **TPXZBM** together with a larger red-shift indicates substantial conformational

relaxation in the excited singlet state in solution which might be associated with slow proton transfer. Because the ^{1}H NMR spectrum and the DFT calculations showed that the keto tautomer of **TPXZBM** is more abundant in the ground state, this conformational relaxation most likely represents conversion of the keto tautomer into the enol tautomer in the singlet excited state, which TD-DFT identified as being significantly more stable. The photoinduced tautomerization implicated in the ESIPT of **TPXZBM** involves a significant conformational rearrangement in order to attain the enol structure, that is the most stable conformer in the first excited state (left hand side of Scheme **1**). However, no significant conformational relaxation should take place in **PXZPDO** since the enol form is the lowest energy tautomer in both the ground and the first excited states. The PL quantum yield (ϕ_{PL}) in degassed toluene is 18% for **PXZPDO**, 1% for **TPXZBM** and 0.2% for **BPXZBM**, which is consistent with the fast PL decay observed in **TPXZBM** and **BPXZBM** on the picosecond time scale, in contrast to **PXZPDO** where no fast decay is observed (Figure **5** and Figure **S29**).

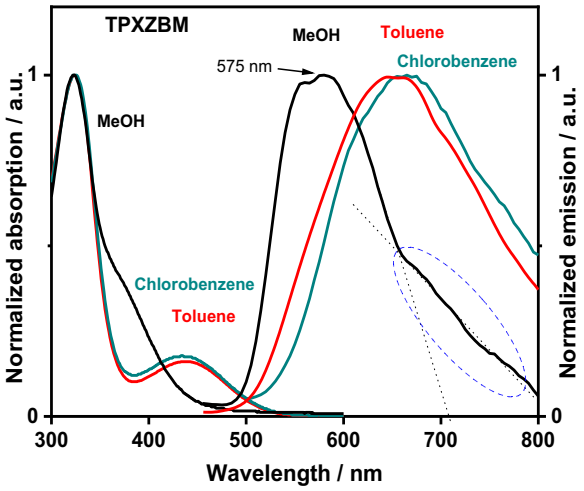

Figure 6. Absorption and photoluminescence spectra of 10^{-3} M **TPXZBM** in methanol and 10^{-5} M **TPXZBM** in toluene and chlorobenzene at room temperature. λ_{exc} = 340 nm.

Further evidence for the photoinduced tautomerization and ESIPT was obtained from the contrast in behavior of the absorption and fluorescence spectra measured in a protic solvent, methanol, *versus* aprotic solvents, toluene and chlorobenzene (Figure **6**). Protic solvents can form intermolecular hydrogen bonds with the acidic proton of the emitter and/or with the oxygen atoms of the emitter, both of which can lead to inhibition of ESIPT and/or hinder the formation of another tautomer and quenching of the emission.[12,39] The absorption spectrum of **TPXZBM** in methanol shows the ICT band maximum at ~380 nm, which is substantially blue-shifted as compared to the same band in toluene and chlorobenzene (~440 nm). This large hypsochromic shift cannot be explained by changes in solvent polarity as the absorption spectra in toluene and chlorobenzene are both very similar despite the different polarities of these two solvents. The shift can likely be explained by the formation of intermolecular H-bonds between methanol to the oxygen atoms of the carbonyl groups of the β-triketone core as illustrated in Scheme **S1**. These intermolecular hydrogen bond interactions stabilize the ground state of the molecule and lead to a larger optical bandgap.[39] This explanation is also consistent with the ^{1}HNMR of **TPXZBM** in CD_3OD, which shows only the presence of the keto tautomer. In comparison, much smaller hypsochromic shifts are observed in the absorption spectra of **PXZPDO** and **BPXZBM** (from 440 nm in toluene to ~420 nm in methanol, Figure **S30**). Compared to **TPXZBM**, **PXZPDO** should hydrogen bond more weakly to methanol as this compound possesses an intramolecular H-bond between the enolic proton and carbonyl oxygen in its most stable enol form; whereas **BPXZBM** does not have an acidic proton and therefore the only intermolecular H-bonding is from the methanol proton to the carbonyl oxygen atoms. The intermolecular H-bonding between methanol and the β-triketone group of **TPXZBM** inhibits ESIPT and causes a large blue-shift of its PL to ~575 nm compared to 650 nm in toluene. With ESIPT significantly suppressed in methanol, the emission occurs

predominantly from the keto tautomer, which is calculated to have a higher energy S_1 state. The long wavelength shoulder observed in the PL spectrum in methanol at around 700 nm has about three times lower intensity than the emission maximum at 575 nm, and most likely represents the enol tautomer, in good agreement with the keto/enol tautomeric ratio in the ground state observed by ^{1}H NMR. The PL spectrum of **TPXZBM** in the other protic solvent, acetic acid, shows a maximum around 550 nm, also indicating inhibition of ESIPT (Figure **S31**). In contrast, the emission of **PXZPDO** in methanol is red-shifted compared to that in the less-polar toluene, which is consistent with the expected positive solvatochromism of ICT excited states (Figure **S30**). We also measured the PL spectra in solutions of varying ratios of toluene:methanol and toluene:acetic acid (Figures **S31-S33**). At low percentages of methanol or acetic acid in toluene the PL maximum of **TPXZBM** showed a red-shift due to increased polarity of the solvent mixture, whilst at higher percentage of these protic solvents the PL maximum shifted to the blue and emission was quenched, indicating ESIPT inhibition. In contrast, **PXZPDO** and **BPXZBM** showed a progressive PL red-shift and quenching with increasing addition of polar protic solvents, consistent with solvation of ICT excited state (Figures **S32-S33**). These results, together with a large dynamic red-shift of the PL maximum of **TPXZBM** in toluene (Figure **5**), suggest that ESIPT is followed by substantial conformational relaxation in solution, but is inhibited in protic solvents.

The PL decays in solution measured by time-correlated single photon counting (TCSPC) are shown in Figures **S34-S36**. Fitting them to biexponential decay function gives a prompt decay component, τ_p of 7.5 ns for **PXZPDO**, 6.9 ns for **TPXZBM** and 6.3 ns for **BPXZBM**, and a delayed component, τ_d, of 0.62 μs for **PXZPDO**, 0.44 μs for **TPXZBM** and 0.43 μs for **BPXZBM.** The prompt and delayed decay times in **PXZPDO** are very similar to those previously reported for this molecule.[24] The TCSPC measurement setup cannot resolve the fast initial decay in

TPXZBM in 20 ps (Figure **5**), hence, the observed decay times correspond to relaxed excited state conformations. The delayed emission is strongly quenched in the presence of oxygen, confirming the TADF nature of the delayed PL component (Figures **S34-S36**).

Photophysical properties in solid matrices

We next investigated the photophysical behavior of these emitters dispersed at 1 wt% in PMMA (Figure **S37**). The absorption spectra are reminiscent of those in toluene with bands observed at 330 and 425 nm. The unstructured PL spectra of the three emitters show λ_{PL} that are much more closely clustered together yet showing the same progressive red-shifting of the emission at 572 nm, 582 nm, and 593 nm for **PXZPDO**, **TPXZBM** and **BPXZBM**, respectively. The Φ_{PL} values are modestly increased compared to those in solution at 35%, 13% and 10% for **PXZPDO**, **TPZXBM** and **BPXZBM**, respectively. Biexponential decay kinetics were observed in the time-resolved decays with τ_p of 15.5, 14.9 and 16.2 ns, and τ_d of 1.07, 1.01and 0.71 μs for **PXZPDO**, **TPXZBM** and **BPXZBM**, respectively (Figure **S38**). These data are consistent with TADF being operative for the emitters in PMMA films.

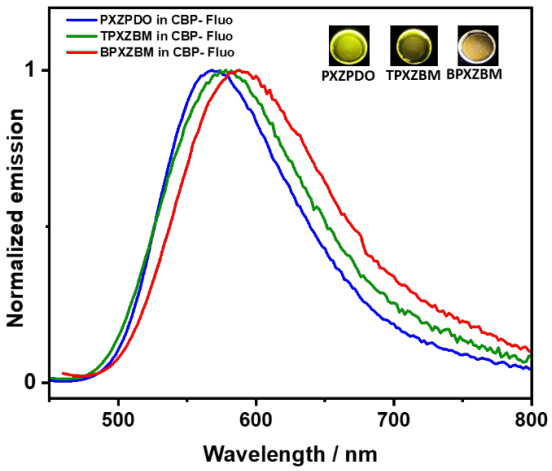

Figure 7. Photoluminescence spectra of emitters dispersed at 1 wt% in CBP matrix at 295 K (λ_{exc} = 340 nm). Photos of photoexcited blends are shown in the inset.

We next investigated the photophysical behavior of the three emitters in an OLED-relevant host, 4,4'-di(9*H*-carbazol-9-yl)-1,1'-biphenyl (CBP), that has a suitably high triplet energy of 2.56 eV.[40] The emitter concentration was optimised in CBP to maximize Φ_{PL} and we found that all emitters show highest Φ_{PL} when doped 1 wt% in CBP. Both the absorption spectra profiles and the values of λ_{PL}, 568 nm, 578nm and 592 nm for **PXZPDO**, **TPXZBM** and **BPXZBM**, respectively (Figure **7** and Figure **S39**), are very similar to those measured in PMMA. This similarity in profile and emission energy between the spectra measured in different hosts suggests that both the nature of the excited state and, for **PXZPDO** and **TPXZBM** the tautomeric form of the emitter, are the same in both media, likely the enol. The Φ_{PL} values in CBP are significantly higher at 58%, 30% and 17% respectively for **PXZPDO**, **TPXZBM** and **BPXZBM** (Table **S5**). The higher Φ_{PL} values in CBP as compared to PMMA can be explained by a higher refractive index of CBP. It is well established that the radiative decays rate k_{rad} is proportional to the refractive index squared.[41] Because $\Phi_{PL}=k_{rad}/k_f$ where k_f is the fluorescence decay rate, and we found that k_f in CBP and PMMA is very similar, hence the expected PLQY in CBP is 1.5 times higher than in PMMA $(1.85/1.49)^2 = 1.5$. It should be noted that the reported Φ_{PL} of the thermally evaporated film of 1 wt% **PXZPDO** in CBP was Φ_{PL} = 68%.[24] The time-resolved PL decays in CBP show a nanosecond prompt emission and a microsecond delayed emission at room temperature (Table **2**) with comparable values to those measured in PMMA. The short delayed lifetime, τ_d, of 1.35, 1.44 and 1.01 μs for **PXZPDO**, **TPXZBM** and **BPXZBM**, respectively, in CBP are expected to contribute to reduced efficiency roll-off in the OLEDs.[6,42,43,44,45] The temperature-dependent time-resolved PL

decays in CBP are shown in Figure **8.** The prompt emission is insensitive to temperature while the delayed emission is thermally activated, a behavior consistent with TADF.

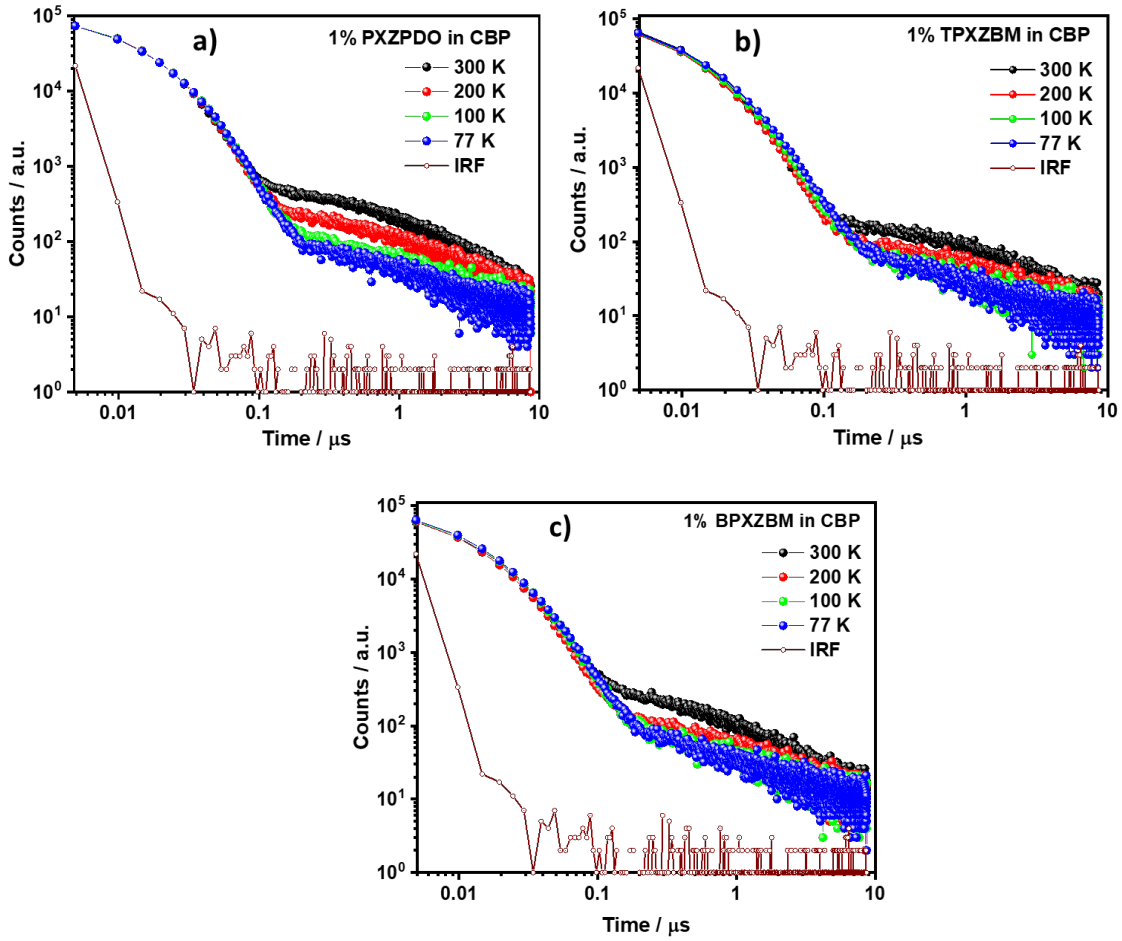

Figure 8. Temperature-dependent photoluminescence decays by TCSPC of 1 wt% CPB doped films of (a) **PXZPDO**; (b) **TPXZBM**; and (c) **BPXZBM**. IRF is the instrument response function (λ_{exc} = 379 nm).

We next measured prompt fluorescence and phosphorescence spectra of the CBP films at 77 K. The energy difference, taken from the onsets of these spectra, provide ΔE_{ST} values of 0.04, 0.02 and 0.005 eV for **PXZPDO**, **TPXZBM** and **BPXZBM**, respectively (Figure **9**, Table **1**). These ΔE_{ST} values are very similar to the DFT-calculated values of **PXZPDO**, the enol tautomer of

TPXZBM, and **BPXZBM**. The calculated ΔE_{ST} for **PXZPDO** in CBP aligns with that previously reported.[24]

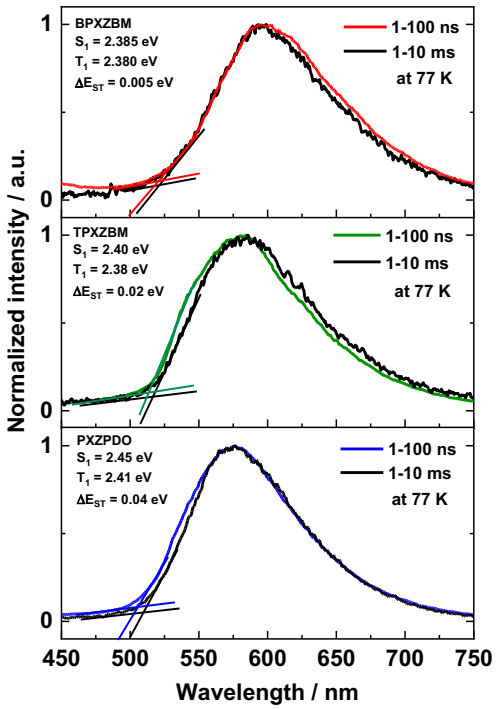

Figure 9. 77 K prompt PL and phosphorescence spectra measurement of 1 wt.% **PXZPDO**, **TPXZBM** and **BPXZBM** doped in CBP host (λ_{exc} = 343 nm), the ΔE_{ST} value is taken from the onset value difference between the 77 K prompt fluorescence and phosphorescence spectra.

In order to clarify the nature of emitting states in the solid matrix we determined and compared the radiative rates of the singlet excited states in CBP matrix and in toluene solutions. These were calculated using $k_r = \Phi_{PF}/\tau_{PF}$ where Φ_{PF} is the quantum yield of the prompt fluorescence and τ_{PF} is the lifetime of prompt fluorescence. The Φ_{PF} corresponds to the percent component of the photoluminescence quantum yield associated with the prompt fluorescence, obtained by integrating the area under the decay curve associated with the prompt fluorescence. The results are given in Table **S6. PXZPDO** and **TPXZBM** in CBP host show very similar k_r values, which

suggests there is a similar nature of the emitting S_1 state in these molecules. The k_r value for **TPXZBM** in toluene solution is about ten times lower than in the solid matrix indicating lower oscillator strength in solution. This is consistent with the decrease of fluorescence intensity on a picosecond timescale (Figure **5**) and can be explained by large conformational relaxation in solution, which is needed to enable the proton transfer in the keto/enol tautomerization. It is worth noting that the PL spectra of **TPXZBM** in frozen glass, where conformational relaxation is suppressed, closely resemble the PL spectrum in CBP, which implies a similar nature of the emitting S_1 state in both (Figure **S40**).

Device characterization

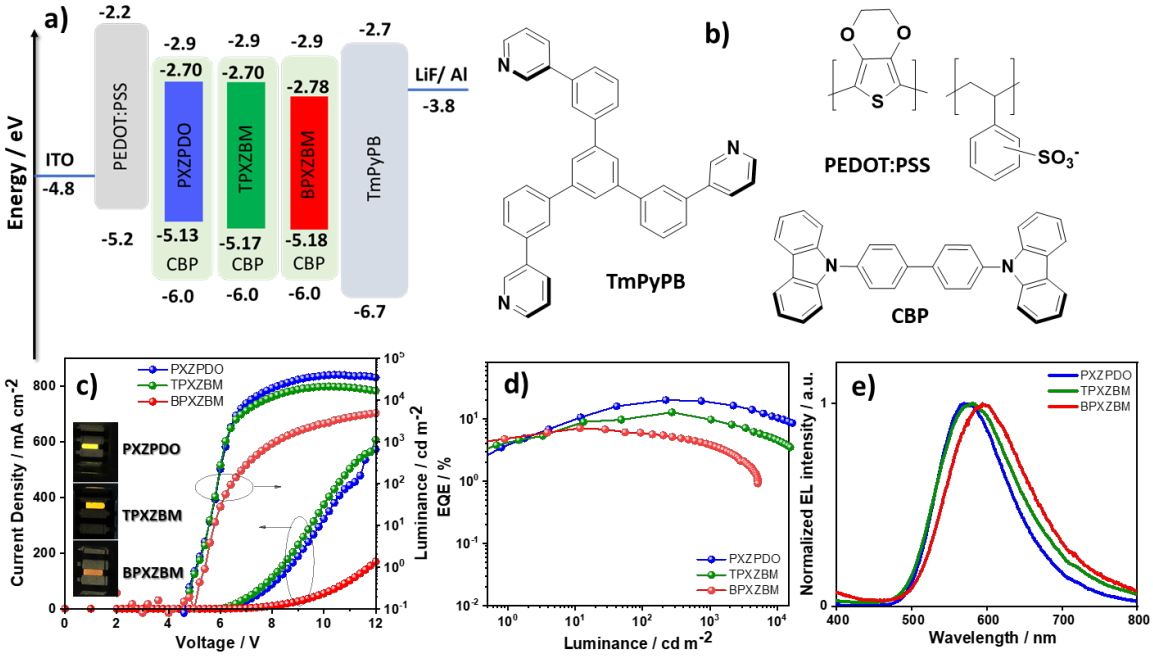

Figure 10. (a) Energy level diagram of materials employed in the devices; (b) Molecular structure of materials used in the devices; (c) Current density and luminescence versus voltage characteristics for the devices, the inset is the electroluminescence of **PXZPDO**, **TPXZBM** and

BPXZBM; (d) External quantum efficiency versus luminescence curves for the devices; (e) Electroluminescence spectra of the device.

The **PXZPDO**-based OLEDs were first fabricated through vacuum deposition using the same device structure as described previously.[24] It can be seen from Figure **S41** that our **PXZPDO** OLED successfully reproduced the performance of the literature device: the EQE_{max} of both OLEDs reached around 18.8% with similar turn-on voltages of 3.4 V. However, due to the high molecular weights of **TPXZBM** and **BPXZBM**, vacuum-deposited films could not be made. Therefore, solution-processed OLEDs were fabricated based on all three emitters. The solution-processed device architecture (Figure **10a**) follows a typical bottom-emitting OLED structure and consists of indium tin oxide (ITO)/poly(3,4-ethylenedioxythiophene):poly(styrenesulfonate) (PEDOT:PSS) (40 nm)/emission layer (35 nm)/1,3,5-tri[(3-pyridyl)-phen-3-yl]benzene (TmPyPB) (80 nm)/LiF (1 nm)/Al (100 nm), where PEDOT:PSS plays the role of both hole injection layer (HIL) and hole transport layer (HTL) and TmPyPB acts both as electron transport layer (ETL) and hole blocking layer due to its deep HOMO (-6.7 eV);[46] the molecular structures of the materials used in these OLEDs are shown in Figure **10b**. The emission layer is composed of 1 wt% of **PXZPDO**, **TPXZBM**, or **BPXZBM** doped into CBP, which was chosen as the host due to the optimized Φ_{PL} (Table **S5**). The performance of the best-performing OLEDs is summarized in Table **3** and device fabrication statistics are provided in Figures **S42-S44**. High EQE_{max} (20.1%) and high maximum current efficiency (CE_{max} = 53.7 cd/A) were still obtained from the solution-processed **PXZPDO** OLED, and its device performance (λ_{EL} = 570 nm, CIE = 0.47, 0.50) is slightly improved compared to our thermally-evaporated device (EQE_{max} = 18.8%, CE_{max} = 57.1 cd/A, λ_{EL} = 560 nm, CIE = 0.44, 0.53, as shown in Figure **S41,** Table **3**).[24] The device EQE is a product of internal quantum efficiency (IQE) and light outcoupling efficiency Φ_{out}. The IQE

of TADF OLED device can be higher than PLQY of thin film because of the Purcell effect of reflective electrodes. Even assuming IQE≈PLQY, the EQE of 20.1 % in a material with 58% PLQY indicates that $\Phi_{out} \approx 0.34$ which is a plausible value for preferential in-plane orientation of the transition dipole moment. Nearly 30% EQE_{max} has been reported, implying a high light outcoupling efficiency.[47]

However, as shown in Figure **10c**, all the solution-processed devices show higher turn-on voltages (~ 5 V) than that of the vacuum-deposited one (3.4 V), which is probably due to the large HOMO value difference between PEDOT:PSS and CBP used in the solution-processed devices. Consequently, the maximum power efficiency, PE_{max}, of our thermal evaporated **PXZPDO** device (52.8 lm/W) is almost double that of our solution-processed one (28.4 lm/W, Figure **S45**). Despite the higher turn-on voltages and lower power efficiency, high EQE_{max} values of 12.7% and 7.0% were obtained from the **TPXZBM** and **BPXZBM** devices with λ_{EL} of 582 nm and 598 nm, respectively (Table **3**). Most importantly, all the devices show low efficiency roll-off at high brightness, as expected. The EQE values dropped by 7.9%, 22.0% and 43.2% at 1000 cd/m^2 for **PXZPDO**, **TPXZBM**, and **BPXZBM**, respectively. This low efficiency roll-off originates in part from the short delayed lifetimes, which contribute to low concentrations of triplet excitons and so lower probability of deleterious triplet-triplet annihilation and triplet-polaron annihilation. Notably, the **PXZPDO** and **TPXZBM** OLEDs are some of a few devices that can reach EQE of > 4% at 10,000 cd/m^2;[42,48] most OLED devices do not reach 10,000 cd/m^2 at all. Although, **BPXZBM** shows a shorter delayed lifetime in comparison to the other two emitters, the device unfortunately exhibits higher efficiency roll-off. A summary of solution-processed TADF-OLEDs emitting beyond 550 nm is given in Table **S7** and compared with our results. All three devices

show broad and structureless EL spectra with λ_{EL} progressively red-shifting from 570 nm (**PXZPDO**) to 582 nm (**TPXZBM**) and to 598 nm (**BPXZBM**), following an analogous trend to their PL spectra, which further supports the conclusion that the EL emission of **TPXZBM** originates from the enol tautomer. The corresponding CIE coordinates are (0.47, 0.50), (0.48, 0.49) and (0.50, 0.46), respectively.

Table 3. Electroluminescence data for the devices

Emitter	*Host*	V_{on}[a] / V	λ_{EL}[b] / nm	*CE*[c] / cd A^{-1}	PE_{max} / lm W^{-1}	*EQE*[c] / %	*CIE*[d] / x,y
PXZPDO	CBP (1%)	5.1 (3.4)[e]	570 (560)[e]	53.7/50.1/27.8 (57.9/49.7/31.7)[e]	28.4 (52.8)[e]	20.1/18.5/10.6 (18.8/16.8/10.8)[e]	0.47, 0.50 (0.44, 0.53)[e]
TPXZBM	CBP (1%)	5.0	582	31.9/24.8/11.6	17.1	12.7/9.9/4.7	0.48, 0.49
BPXZBM	CBP (1%)	5.4	598	15.5/8.5/-	8.4	7.05/4.0/ -	0.50, 0.46

[a] The turn-on voltage at a brightness 1 cd m^{-2}. [b] The electroluminescence maximum recorded at 8 V. [c] The order of measured value: the maximum, then values at 1000 and 10,000 cd m^{-2}. [d] The CIE coordinates recorded at 8 V. [e] Thermally evaporated OLEDs performance. Values in parentheses are for thermally evaporated device.

CONCLUSION:

In summary, we report a rare example of a TADF emitter **TPXZBM** that also exhibits two types of tautomeric equilibria: i) a slow one between a keto form (more stable in the ground state) and an enol form (favoured in the excited-state); ii) a fast one between two equivalent tautomers in the enol form. This system is fundamentally different from previous structures based on intramolecular proton transfer, in which only one of the two types of tautomerism was present. This TADF compound was used as the emitter in a solution-processed OLED, and it shows a small ΔE_{ST} (0.04 eV for enol tautomer) and a short delayed lifetime. For comparison we synthesized the previously reported **PXZPDO**, which shows only fast proton transfer (in both states), and the reference molecule **BPXZBM** where no proton transfer is possible. Solution-processed OLEDs based on

PXZPDO, **TPXZBM** and **BPXZBM** emitters without a hole transporting layer exhibited EQE_{max} 20.1%, 12.7% and 7.0%, with emission peaking in the yellow/orange/red colour range of the spectrum. Many TADF materials suffer a severe efficiency roll-off at high brightness; however, at a very high brightness of 10,000 cd/m^2 **PXZPDO** and **TPXZBM** maintained good EQEs of 10.6% and 4.7%, respectively, demonstrating relatively low efficiency roll off which we see rarely in solution processed devices. We also find that **PXZPDO** has the best efficiency of emitters that can be processed from either vacuum or solution with electroluminescence spectrum at above 560 nm. This is the first report of a solution-processed TADF OLED with intramolecular proton transfer, and our results suggest this is a useful approach for developing materials with low efficiency roll-off.

EXPERIMENTAL SECTION:

General Synthetic Procedures.

All the commercially available chemicals and reagent grade solvents were used as received. Air-sensitive reactions were performed under a nitrogen atmosphere using Schlenk techniques. Flash column chromatography was carried out using silica gel (Silia-P from Silicycle, 60 Å, 40-63 μm). Analytical thin-layer-chromatography (TLC) was performed with silica plates with aluminium backings (250 μm with F-254 indicator). TLC visualization was accomplished by 254/365 nm UV lamp. ^{1}H and ^{13}C NMR spectra were recorded on a Bruker Advance spectrometer (400 MHz, 500 MHz for ^{1}H and 126 MHz for ^{13}C). Melting points were measured using open-ended capillaries on an Electrothermal melting point apparatus and are uncorrected. High-resolution mass spectrometry (HRMS) was performed by EPSRC National Mass Spectrometry Service Centre (NMSSC),

Swansea. Elemental analyses were performed by Mr. Stephen Boyer, London Metropolitan University.

Synthesis of 1,3-bis(4-bromophenyl)-3-hydroxypropan-1-one (DBrPDO). The intermediate product 1,3-bis(4-bromophenyl)-3-hydroxypropan-1-one **(DBrPDO)** was synthesized according to the reported procedure.[49] Colorless crystals. **Yield**: 74%. Mp: 188 -193 °C. **^{1}H NMR (400 MHz, Chloroform-*d*) δ (ppm):** 16.74 (s, 1H), 7.88 – 7.83 (m, 4H), 7.67 – 7.63 (m, 4H), 6.77 (s, 1H). **^{13}C NMR (126 MHz, DMSO-d_6) δ (ppm)**: 184.80, 134.07, 132.42, 129.95, 127.66, 93.97. ^{1}H NMR matches that of the literature.[49]

Synthesis of 2-(4-bromo benzoyl)-1,3-bis(4-bromophenyl)propane-1,3-dione (TBrPDO). The synthesis of (**TBrPDO**) was adapted from the literature.[29] To 1,3-bis(4-bromophenyl)-3-hydroxypropan-1-one (**DBrPDO**) (3.50 g 9.1 mmol, 1 equiv.) was added diethylether (50 mL) and the reaction mixture was stirred at 0 °C under N_2 atmosphere for 10 min. NaH (60% in oil, 0.38 g, 9.6 mmol, 1.05 equiv.) was added to the reaction mixture and the reaction mixture was stirring for 15 min at 0 °C. The reaction was then allowed to warm to room temperature for 2 h. To this reaction mixture has added dropwise a solution of 4-bromobenzoyl chloride (2.11 g, 9.6 mmol, 1.05 equiv.) in diethyl ether (30 mL). The reaction mixture was then stirred for 15 h at room temperature. The reaction was quenched by the addition of two drops of ethanol and 1N HCl such that the pH of the reaction mixture was 2 and the final product was precipitated out. The precipitate was filtered and washed with water (5 × 50 mL). The product was recrystallized from dichloromethane and acetonitrile (1:4) and then filtered and dried under vacuum to afford a white, flaky compound. **Yield**: 2.34 gm, 45%. **Mp**: 236-240°C. **^{1}H NMR (500 MHz, DMSO-d_6) δ (ppm)**: 8.12 (s, 1H), 7.93 (d, J = 8.7 Hz, 6H), 7.81 (d, J = 8.6 Hz, 6H). **^{13}C NMR (126 MHz, DMSO-d_6) δ (ppm)**: 192.82, 134.08, 132.11, 130.49, 128.53, 65.06. **HR ESI-MS: [M - H]$^-$:** calcd for [$C_{22}H_{13}Br_3O_3$ -

H]$^-$: 562.8314, found: 562.8319. **Elemental analysis:** Calcd for $C_{22}H_{13}Br_3O_3$: C, 46.76; H, 2.32 Found: C, 46.83; H, 2.34.

Synthesis of 1,3-bis(4-(10Hphenoxazin-10-yl)phenyl)-3-hydroxyprop-2-en-1-one (PXZPDO). The compound **PXZPDO** was synthesized according to the literature.[24] Red powder, **Yield**: 80%. **Mp**: 257-260 °C. **^{1}H NMR (400 MHz, Chloroform-*d*) δ (ppm)**: 16.83 (s, 1H), 8.24 (d, *J* = 8.1 Hz, 4H), 7.52 (d, *J* = 8.1 Hz, 4H), 6.95 (s, 1H), 6.72 (t, *J* = 10.4 Hz, 8H), 6.62 (t, *J* = 7.6 Hz, 4H), 5.99 (d, *J* = 7.8 Hz, 4H). **^{13}C NMR (126 MHz, Chloroform-*d*) δ (ppm)**:184.98, 144.11, 143.28, 135.41, 133.86, 131.37, 130.13, 123.44, 121.98, 115.86, 113.43, 93.75. **HR ESI-MS: [M]$^+$:** calcd for $[C_{39}H_{26}N_2O_4]^+$: 586.1893, found: 586.1884. **Elemental analysis:** Calcd for $C_{39}H_{26}N_2O_4$: C, 79.85; H, 4.47; N, 4.78. Found: C, 79.71; H, 4.57; N, 4.75. ^{1}H NMR, ^{13}C NMR, ESI-MS and elemental analysis match that reported in the literature.[24]

Synthesis of Tris(4-(10H-phenoxazin-10-yl)benzoyl)methane (TPXZBM). A mixture of **TBrPDO** (0.500 g, 0.884 mmol, 1.0 equiv.), 10H-phenoxazine (0.534 gm, 2.92 mmol, 3.3 equiv.), Cs_2CO_3 (0.951 g, 2.92 mmol, 3.3 equiv.) and toluene (30 mL) were taken in a dried Schlenk flask and purged with N_2 with constant stirring for 1 h. To a second dried Schlenk flask was added $[Pd(OAc)_2]_3$ (0.020 g, 0.029 mmol, 3.3% with respect to **TBrPDO**), tri-*tert*-butylphosphonium tetrafluoroborate (0.076 g, 0.261 mmol, 9 equiv. with respect to $[Pd(OAc)_2]_3$) and toluene (10 mL) and the mixture was stirred for 1 h under a N_2 atmosphere. After 1 h, the brownish-yellow colored solution of the Pd-complex was added to the **TBrPDO**-containing reaction mixture. The reaction mixture was stirred at 110 °C for 20 h. The yellow colored reaction mixture was cooled to room temperature and the reaction was quenched with brine (50 mL). The reaction mixture was extracted with CH_2Cl_2 (100 mL) and washed several times with water (4 × 100 mL) and dried over anhydrous Na_2SO_4. The product was recrystallization from hot dichloromethane (DCM) and

acetonitrile (MeCN) in a ratio of 2:5. The orange precipitate was filtered, washed with acetonitrile and diethyl ether and dried under vacuum. A second recrystallization from a DCM and MeCN (2:5) mixture by slow evaporation yielded the title compound crystal for SCXRD. **Yield**: 0.540 gm 70%. **R_f:** 0.16 (hexane: DCM = 7:3 on silica gel). **Mp**: 291°C - 295°C. **^{1}H NMR (400 MHz, Chloroform-*d*) δ (ppm)**: 8.20 (d, *J* = 8.5 Hz, 6H), 7.54 (d, *J* = 8.5 Hz, 6H), 7.20 (s, 1H), 6.72 (qd, *J* = 7.9, 1.5 Hz, 12H), 6.63 (td, *J* = 7.6, 2.0 Hz, 6H), 6.03 (d, *J* = 7.7 Hz, 6H). **^{13}C NMR (126 MHz, DMSO) δ (ppm)**: 193.21, 143.94, 143.35, 135.05, 133.14, 131.84, 131.12, 123.88, 122.15, 115.65, 113.63, 65.57. **HR ESI-MS: [M - H]$^-$:** calcd for [$C_{58}H_{37}N_3O_6$ - H]$^-$: 870.2602, found: 870.2614. **Elemental analysis:** Calcd for $C_{58}H_{37}N_3O_6$: C, 79.89; H, 4.28; N, 4.82. Found: C, 79.73; H, 4.23; N, 4.57.

Synthesis of bis-(4-bromobenzoyl)bis-(4-(10H-phenoxazin-10-yl)benzoyl)methane (BPXZBM). To **PXZPDO** (0.700 g, 1.19 mmol, 1.0 equiv.) was added diethyl ether (30 mL) and the solution was cooled to 0 °C and stirred for 10 min under nitrogen. To the reaction mixture was added NaH (60% in oil) (0.095 g 2.38 mmol, 2.0 equiv.). The reaction was stirred for 3 h at which point the color of the reaction mixture changed from red to yellowish orange. To the reaction mixture was slowly added 4-Br-benzoylchloride (0.522 g 2.38 mmol, 2.0 equiv.) in diethyl ether (20 mL). The reaction was stirred for 15 h. After 15 h the color of the reaction mixture converted to dark orange. The reaction was quenched by addition of 2 drops of ethanol and 10 mL water. 1 N HCl was added to the reaction mixture to maintain the pH = 2. The product was extracted with DCM (80 mL) and washed with water (4 × 50 mL). The product solution was concentrated under reduced pressure and the product was then purified by column chromatography, **R_f:** 0.23 (hexane:DCM = 7:3 on silica gel). **Mp**: 144-150°C. dark orange powder **Yield**: 0.85 g, 75 %.**^{1}H NMR (500 MHz, CD_2Cl_2) δ (ppm):** 8.26 (d, *J* = 8.4 Hz, 2H), 8.16 (d, *J* = 8.5 Hz, 1H), 7.89 (dd, *J* = 8.6, 2.6 Hz, 1H), 7.77

(d, J = 8.6 Hz, 1H), 7.73 – 7.66 (m, 2H), 7.65 – 7.55 (m, 4H), 7.43 (t, J = 8.2 Hz, 3H), 7.36 – 7.30 (m, 2H), 7.23 (d, J = 8.5 Hz, 1H), 6.67 (dt, J = 18.1, 2.8 Hz, 9H), 6.57 – 6.51 (m, 2H), 5.75 (d, J = 8.4 Hz, 1H), 5.64 (t, J = 8.3 Hz, 2H), 5.54 – 5.51 (m, 1H). **^{13}C NMR (101 MHz, CD_2Cl_2) δ (ppm)**: 192.67, 143.98, 135.62, 133.46, 132.22, 132.02, 131.49, 131.12, 131.04, 130.94, 130.03, 123.31, 121.86, 115.55, 113.18, 112.94 **HR ESI-MS: $[M + H]^+$:** calcd for $[C_{53}H_{32}Br_2N_2O_6H]^+$: 953.0685, found: 953.0690. **Elemental analysis:** Calcd for $C_{53}H_{32}Br_2N_2O_6$: C, 66.82; H, 3.39; N, 2.94. Found: C, 66.72; H, 3.36; N, 2.82.

DFT calculations

To perform our calculations, we used the Gaussian 16.A03 code,[50] applying default procedures, algorithms and thresholds except when noted below. The ground and excited states have been modelled with DFT and TD-DFT, respectively using the PBE0 global hybrid functional.[51] For each state, we performed geometry optimization and analytical frequency calculations selecting the 6-31G(d) atomic basis set, the *ultrafine* integration grid, and imposing improved convergence thresholds for both the SCF (10^{-10} au) and residual forces (10^{-5} au). The solvent effects (here toluene) were accounted for at all steps using the well-known PCM model.[52] As expected, all minima show zero imaginary frequency, whereas the PT transfer transition states, that were located as well, show a high-frequency imaginary mode corresponding to the OH stretching. Single points calculations with a larger basis set, namely 6-311+G(2d,p), were performed on the minimized structures, so that the transition energies were obtained with that basis set, using the linear-response model for the PCM step.

Electrochemistry

Cyclic Voltammetry (CV) and Differential pulse voltammetry (DPV) analysis was performed on an Electrochemical Analyzer potentiostat model 620D from CH Instruments. Samples were prepared in dichloromethane (DCM) solutions, which were degassed by sparging with DCM-saturated nitrogen gas for 5 minutes prior to measurements. All measurements were performed using 0.1M tetra-*n*-butylammonium hexafluorophosphate, [nBu$_4$N]PF$_6$], in DCM at scan rate of 100 mV s^{-1}. An Ag/Ag$^+$ electrode was used as the reference electrode, a platinum electrode was used as the working electrode and a platinum wire was used as the counter electrode. The redox potentials are reported relative to a saturated calomel electrode (SCE) with a ferrocene/ferrocenium/ (F_c/F_c^+) redox couple as the internal standard (0.46 V vs SCE).[34] The HOMO and LUMO energies were determined using $E_{HOMO} = -(E_{ox} + 4.8)eV$,[35] where E_{ox} is anodic peak potentials, respectively calculated from DPV relative to F_c/F_c^+ and $E_{LUMO} = |E_{HOMO} - E_g|$, E_g is optical band gap obtained from the intersection of the normalised absorption and emission spectra in PhMe.

Photophysical measurements

Photophysics in the solution

Solution samples were prepared using HPLC-grade solvents with varying concentrations on the order of 10^{-5} M for absorption and emission studies, respectively. Solutions were put into quartz cuvettes for all the photophysics measurements. Aerated solutions were prepared by bubbling with compressed air for 5 minutes whereas degassed solutions were prepared via three freeze-pump-thaw cycles prior to emission and life-time analysis using an in-house adapted fluorescence cuvette, itself purchased from Starna. Absorption spectra were recorded at RT using a CARY 300 Bio. Molar absorptivity values were determined from at least four solutions followed by linear

regression analysis. To dissolve the **TPXZMB** in any solvents, the solution mixtures were heated upto 60-70 ^{o}C. Before measuring the photophysics of all emitters in methanol, the solutions were sonicated for two minutes and heated. For measuring PL spectra of all emitters in solutions varying the ratio of toluene:methanol and toluene:acetic acid volume, we mixed solvents (toluene:methanol and toluene:acetic acid) with ratio 100:0, 75:25, 50:50, 25:75 and 0:100 and prepared 10^{-5} M solutions of each emitters separately.

Photophysics in the solid state

Samples for PL decay measurements were prepared by spin-coating a thin film from chloroform (Sigma Aldrich, HPLC grade) at 2000 RPM in ambient environment on quartz substrates and annealed at 65 ^{o}C for 10 min. The films for ΔE_{ST} measurements were prepared by drop casting a chloroform solution on cleaned sapphire substrates and annealed at 160-180 ^{o}C for 1 min under N_2 atmosphere to obtain a sufficiently homogeneous thick film in order to acquire sufficient signal for the phosphorescence. Film samples for PLQY measurement were spin coated.

Steady-state emission and time-resolved PL decay

Steady-state and time-resolved emission spectra were recorded at 298 K using an Edinburgh Instruments F980 fluorimeter in an oxygen free atmosphere. All the samples for the steady-state measurements were excited at 340 nm using a Xenon lamp, while the samples for the time-resolved measurements were excited at 378 nm using a pico-second laser (PicoQuant, LDH-D-C-375) driven by a laser driver (PDL 800-D). PL decays were measured using time-correlated single photon counting (TCSPC) mode and data was fitted with respect to instrument response function (IRF).

Photoluminescence quantum yields (PLQY) in solution

Photoluminescence quantum yields for solutions were determined using the optically dilute method[36] in which four sample solutions with absorbance of ca. 0.150, 0.125, 0.100 and 0.075 at 448 nm were used. Their emission intensities were compared with those of a reference, tris(bipyridine)ruthenium(II) chloride, whose quantum yield (Φ_r) in H_2O was determined to be 2.8 % using absolute method.[37] The quantum yield of the sample, Φ_{PL}, can be determined by the equation $\Phi_{PL} = \Phi_r(A_r/A_s)(I_s/I_r)(n_s/n_r)^2$, where A stands for the absorbance at the excitation wavelength (λ_{exc} = 448 nm), I is the integrated area under the corrected emission curve and n is the refractive index of the solvent with the subscripts "s" and "r" representing sample and reference respectively.

Photoluminescence quantum yields (PLQY) in solid thin film

A Hamamatsu C9920-02 integrating sphere was employed for PLQY measurements for thin film samples.[53] A xenon lamp coupled to a monochromator enabled selective excitation chosen here to be 300 nm for CBP thin films and 420 nm for PMMA thin films. The output was then fed into the integrating sphere via a fiber, exciting the sample. PL spectra were collected with a multimode fiber and detected with a back-thinned CCD under a nitrogen or oxygen atmosphere as required.

ΔE_{ST} measurement.

The singlet-triplet splitting energy, ΔE_{ST}, was estimated by recording the prompt fluorescence and the delayed phosphorescence spectra at 77 K. The film for ΔE_{ST} measurement were prepared through drop casting of a 1 wt% emitters in 4,4′-Bis(N-carbazolyl)-1,1′-biphenyl (CBP) host chloroform solution on cleaned sapphire substrates. All samples were loaded inside a cold finger

cryostat (Oxford Instruments) for vacuum condition and 300 K – 77 K temperature control. All samples were photoexcited using the third harmonic emission (343 nm) from a femtosecond laser which originally emits at 1030 nm (Orpheus-N, model: PN13F1). Emission from the samples was focused onto a spectrograph (Chromex imaging, 250 is spectrograph) and detected with a sensitive gated iCCD camera (Stanford Computer Optics, 4Picos) having sub-nanosecond resolution. Prompt fluorescence spectra were integrated by iCDD between 1 ns – 100 ns after the laser excitation. Phosphorescence spectra were integrated by iCDD between 1– 10 ms after the laser excitation. The energy values of the lowest singlet and triplet states were determined from the onset of fluorescence spectrum at 77 K and phosphorescence spectrum at 77 K.

k_r rates measurement.

The decay times of prompt and delayed fluorescence were obtained using two-exponential fits and are given in Table **2**. The contribution of prompt fluorescence to total PLQY was estimated using equation 1.

$$PLQY_{prompt} = \frac{PLQY_{total} a_P \tau_P}{a_P \tau_P + a_D \tau_D} \qquad (1)$$

where τ_P and τ_D are the decay times of prompt and delayed fluorescence obtained by fitting the decays with two-exponential decay function convolved with the instrument response function (IRF), whilst a_P and a_D are the pre-exponential factors of these fits. We determined the radiative rate of S_1 state using $k_r = \frac{PLQY_{prompt}}{\tau_P}$. Then the rate constants of ISC (k_{ISC}) was estimated using previously derived equations[54]

$$k_{ISC} = \frac{1-PLQY_{prompt}}{\tau_P} \qquad (2)$$

where $PLQY_{Delayed}=PLQY_{total} - PLQY_{Prompt}$. Here the assumption is made that non-radiative losses from S_1 are negligible. Higher k_r rates are preferential for OLEDs because they facilitate faster conversion of excited triplet states into photons, hence they reduce the efficiency roll-off at high current densities. Both rates are found to be higher in **PXZPDO** as compared to **TPXZBM** and **BPXZBM** (Table **S6**).

Time resolved picosecond lifetime measurement.

Time-resolved fluorescence spectra on a picosecond time scale were measured with a Hamamatsu streak camera in synchroscan mode coupled to a spectrograph. Excitation was by 200 fs pulses at a pulse repetition rate of 200 kHz. Different excitation wavelength in the range from 400 nm to 460 nm were tested and were found to give very similar fluorescence spectra.

OLED fabrication and characterization

OLED devices were fabricated in bottom emitting architecture on indium doped tin oxide (ITO, 12 mm × 12 mm × 1.1 mm, resistivity: 15 Ω/sq) substrates. Substrates were washed sequentially by ultrasonication in DCM, acetone, and isopropanol for 15 min and then exposed to oxygen plasma for 10 min to remove all the dust and organics on the ITO surface. The hole injection layer poly(3,4-ethylenedioxythiophene):poly(styrenesulfonate) (PEDOT:PSS, Heraeus, Clevios P VP. AI 4083, charge:9001157883) were spin-coated onto ITO surface under 4000 rpm for 1 min then transferred all substrates inside nitrogen filled glove box and baked at 130 °C for 15 min to remove the residual water. The emitting layer (1% emitter: 99% CBP in $CHCl_3$) was spin-coated under

2000 rpm (40 nm) and annealed at 65 °C after the substrate was transferred into a nitrogen filled glove box. The electron transporting layer (1,3,5-tri[(3pyridyl)-phen-3-yl]benzene, TmPyPB, 80 nm), the electron injecting layer (lithium fluoride, LiF 1 nm) and aluminium cathode (100 nm) were successively thermally evaporated in a vacuum chamber under < 1×10^{-6} mbar. After the evaporation, the OLEDs were taken out from the evaporator and encapsulated inside the glovebox. Then, they were taken out from the glovebox for current-voltage-luminance characteristics. This characterization was performed using a source meter (Keithley 2400) combined with a homemade photodiode connected to a multimeter (Keithley 2000) for the voltage reading. The spectrum was collected by an optical fiber connected to a spectrometer (Andor, Model Number: DV420-BV). External quantum efficiency (EQE) calculation were done based on the assumption that the emission patterns of the OLEDs are Lambertian. The OLED active areas were around 4 mm^2. We calculated EQE values dropped by using equation $EQE_{dropped\ values} = (EQE_{max} - EQE_{1000\ cd\ /m^2})/(EQE_{max}) \times 100$.

ASSOCIATED CONTENT:

Supporting Information

Compound characterization (^{1}H NMR, ^{13}C NMR, elemental analysis, HRMS), SCXRD, photophysical studies, OLEDs data, DFT calculations, literature survey of solution process OLEDs with electroluminescence at above 560 nm. The following files are available free of charge. Crystallographic information of **TPXZBM** (via CCDC: 2033769).

AUTHOR INFORMATION:

Corresponding Author

Eli Zysman-Colman - E-mail: eli.zysman-colman@st-andrews.ac.uk (EZC)

Ifor D. W. Samuel - E-mail: idws@st-andrews.ac.uk (IDWS)

Denis Jacquemin – E-mail: denis.jacquemin@univ-nantes.fr (DJ)

ACKNOWLEDGMENT:

AKG is grateful to the Royal Society for Newton International Fellowship NF171163. We acknowledge support from the Engineering and Physical Sciences Research Council of the UK (grants EP/P010482/1 and EP/L017008/1). We thank the EPSRC UK National Mass Spectrometry Facility at Swansea University for analytical services. We thank Umicore for providing palladium (II) acetate. DJ thanks the CCIPL computational centre installed in Nantes for generous allocation of computational resources.

REFERENCES

(1) Kaji, H.; Suzuki, H.; Fukushima, T.; Shizu, K.; Suzuki, K.; Kubo, S.; Komino, T.; Oiwa, H.; Suzuki, F.; Wakamiya, A.; Murata, Y.; Adachi, C. Purely Organic Electroluminescent Material Realizing 100% Conversion from Electricity to Light. *Nat. Commun.* **2015**, *6* (May), 2–9. https://doi.org/10.1038/ncomms9476.

(2) Wong, M. Y.; Zysman-Colman, E. Purely Organic Thermally Activated Delayed Fluorescence Materials for Organic Light-Emitting Diodes. *Adv. Mater.* **2017**, *29* (22), 1605444. https://doi.org/10.1002/adma.201605444.

(3) Yang, Z.; Mao, Z.; Xie, Z.; Zhang, Y.; Liu, S.; Zhao, J.; Xu, J.; Chi, Z.; Aldred, M. P. Recent Advances in Organic Thermally Activated Delayed Fluorescence Materials. *Chem. Soc. Rev.* **2017**, *46* (3), 915–1016. https://doi.org/10.1039/c6cs00368k.

(4) Liu, Y.; Li, C.; Ren, Z.; Yan, S.; Bryce, M. R. All-Organic Thermally Activated Delayed

Fluorescence Materials for Organic Light-Emitting Diodes. *Nat. Rev. Mater.* **2018**, *3*. https://doi.org/10.1038/natrevmats.2018.20.

(5) Uoyama, H.; Goushi, K.; Shizu, K.; Nomura, H.; Adachi, C. Highly Efficient Organic Light-Emitting Diodes from Delayed Fluorescence. *Nature* **2012**, *492* (7428), 234–238. https://doi.org/10.1038/nature11687.

(6) Zhang, Q.; Li, B.; Huang, S.; Nomura, H.; Tanaka, H.; Adachi, C. Efficient Blue Organic Light-Emitting Diodes Employing Thermally Activated Delayed Fluorescence. *Nat. Photonics* **2014**, *8* (4), 326–332. https://doi.org/10.1038/nphoton.2014.12.

(7) Hatakeyama, T.; Shiren, K.; Nakajima, K.; Nomura, S.; Nakatsuka, S.; Kinoshita, K.; Ni, J.; Ono, Y.; Ikuta, T. Ultrapure Blue Thermally Activated Delayed Fluorescence Molecules: Efficient HOMO-LUMO Separation by the Multiple Resonance Effect. *Adv. Mater.* **2016**, *28* (14), 2777–2781. https://doi.org/10.1002/adma.201505491.

(8) Gan, L.; Xu, Z.; Wang, Z.; Li, B.; Li, W.; Cai, X.; Liu, K.; Liang, Q.; Su, S. J. Utilizing a Spiro TADF Moiety as a Functional Electron Donor in TADF Molecular Design toward Efficient "Multichannel" Reverse Intersystem Crossing. *Adv. Funct. Mater.* **2019**, *29* (20), 1–8. https://doi.org/10.1002/adfm.201808088.

(9) Sarma, M.; Wong, K. T. Exciplex: An Intermolecular Charge-Transfer Approach for TADF. *ACS Appl. Mater. Interfaces* **2018**, *10* (23), 19279–19304. https://doi.org/10.1021/acsami.7b18318.

(10) Spuling, E.; Sharma, N.; Samuel, I. D. W.; Zysman-Colman, E.; Bräse, S. (Deep) Blue through-Space Conjugated TADF Emitters Based on [2.2]Paracyclophanes. *Chem.*

Commun. **2018**, *54* (67), 9278–9281. https://doi.org/10.1039/c8cc04594a.

(11) Mamada, M.; Inada, K.; Komino, T.; Potscavage, W. J.; Nakanotani, H.; Adachi, C. Highly Efficient Thermally Activated Delayed Fluorescence from an Excited-State Intramolecular Proton Transfer System. *ACS Cent. Sci.* **2017**, *3* (7), 769–777. https://doi.org/10.1021/acscentsci.7b00183.

(12) Padalkar, V. S.; Seki, S. Excited-State Intramolecular Proton-Transfer (ESIPT)-Inspired Solid State Emitters. *Chem. Soc. Rev.* **2016**, *45* (1), 169–202. https://doi.org/10.1039/c5cs00543d.

(13) Sedgwick, A. C.; Wu, L.; Han, H. H.; Bull, S. D.; He, X. P.; James, T. D.; Sessler, J. L.; Tang, B. Z.; Tian, H.; Yoon, J. Excited-State Intramolecular Proton-Transfer (ESIPT) Based Fluorescence Sensors and Imaging Agents. *Chem. Soc. Rev.* **2018**, *47* (23), 8842–8880. https://doi.org/10.1039/c8cs00185e.

(14) Gupta, A. K.; Kumar, A.; Singh, R.; Devi, M.; Dhir, A.; Pradeep, C. P. Facile Synthesis of an Organic Solid State Near-Infrared-Emitter with Large Stokes Shift via Excited-State Intramolecular Proton Transfer. *ACS Omega* **2018**, *3* (10), 14341–14348. https://doi.org/10.1021/acsomega.8b02116.

(15) Singh, R.; Gupta, A. K.; Pradeep, C. P. Synthesis of a New Series of Organic Solid-State Near-Infrared Emitters: The Role of Crystal Packing and Weak Intermolecular Interactions and Application in Latent Fingerprint Detection. *Cryst. Growth Des.* **2021**, acs.cgd.0c01392. https://doi.org/10.1021/acs.cgd.0c01392.

(16) Yao, D.; Zhao, S.; Guo, J.; Zhang, Z.; Zhang, H.; Liu, Y.; Wang, Y. Hydroxyphenyl-

Benzothiazole Based Full Color Organic Emitting Materials Generated by Facile Molecular Modification. *J. Mater. Chem.* **2011**, *21* (11), 3568–3570. https://doi.org/10.1039/c1jm00009h.

(17) Tang, K. C.; Chang, M. J.; Lin, T. Y.; Pan, H. A.; Fang, T. C.; Chen, K. Y.; Hung, W. Y.; Hsu, Y. H.; Chou, P. T. Fine Tuning the Energetics of Excited-State Intramolecular Proton Transfer (ESIPT): White Light Generation in a Single ESIPT System. *J. Am. Chem. Soc.* **2011**, *133* (44), 17738–17745. https://doi.org/10.1021/ja2062693.

(18) Chuang, W. T.; Hsieh, C. C.; Lai, C. H.; Lai, C. H.; Shih, C. W.; Chen, K. Y.; Hung, W. Y.; Hsu, Y. H.; Chou, P. T. Excited-State Intramolecular Proton Transfer Molecules Bearing o -Hydroxy Analogues of Green Fluorescent Protein Chromophore. *J. Org. Chem.* **2011**, *76* (20), 8189–8202. https://doi.org/10.1021/jo2012384.

(19) Cai, M.; Gao, Z.; Zhou, X.; Wang, X.; Chen, S.; Zhao, Y.; Qian, Y.; Shi, N.; Mi, B.; Xie, L.; Huang, W. A Small Change in Molecular Structure, a Big Difference in the AIEE Mechanism. *Phys. Chem. Chem. Phys.* **2012**, *14* (15), 5289–5296. https://doi.org/10.1039/c2cp23040b.

(20) Zhang, Z.; Chen, Y. A.; Hung, W. Y.; Tang, W. F.; Hsu, Y. H.; Chen, C. L.; Meng, F. Y.; Chou, P. T. Control of the Reversibility of Excited-State Intramolecular Proton Transfer (ESIPT) Reaction: Host-Polarity Tuning White Organic Light Emitting Diode on a New Thiazolo[5,4-d]Thiazole ESIPT System. *Chem. Mater.* **2016**, *28* (23), 8815–8824. https://doi.org/10.1021/acs.chemmater.6b04707.

(21) Duarte, L. G. T. A.; Germino, J. C.; Berbigier, J. F.; Barboza, C. A.; Faleiros, M. M.; De

Alencar Simoni, D.; Galante, M. T.; De Holanda, M. S.; Rodembusch, F. S.; Atvars, T. D. Z. White-Light Generation from All-Solution-Processed OLEDs Using a Benzothiazole-Salophen Derivative Reactive to the ESIPT Process. *Phys. Chem. Chem. Phys.* **2019**, *21* (3), 1172–1182. https://doi.org/10.1039/c8cp06485g.

(22) Li, B.; Tang, G.; Zhou, L.; Wu, D.; Lan, J.; Zhou, L.; Lu, Z.; You, J. Unexpected Sole Enol-Form Emission of 2-(2′-Hydroxyphenyl)Oxazoles for Highly Efficient Deep-Blue-Emitting Organic Electroluminescent Devices. *Adv. Funct. Mater.* **2017**, *27* (9), 1605245. https://doi.org/10.1002/adfm.201605245.

(23) Park, S.; Kwon, O. H.; Lee, Y. S.; Jang, D. J.; Park, S. Y. Imidazole-Based Excited-State Intramolecular Proton-Transfer (ESIPT) Materials: Observation of Thermally Activated Delayed Fluorescence (TDF). *J. Phys. Chem. A* **2007**, *111* (39), 9649–9653. https://doi.org/10.1021/jp072212p.

(24) Wu, K.; Zhang, T.; Wang, Z.; Wang, L.; Zhan, L.; Gong, S.; Zhong, C.; Lu, Z. H.; Zhang, S.; Yang, C. De Novo Design of Excited-State Intramolecular Proton Transfer Emitters via a Thermally Activated Delayed Fluorescence Channel. *J. Am. Chem. Soc.* **2018**, *140* (28), 8877–8886. https://doi.org/10.1021/jacs.8b04795.

(25) Van Klink, J. W.; Brophy, J. J.; Perry, N. B.; Weavers, R. T. β-Triketones from Myrtaceae: Isoleptospermone from Leptospermum Scoparium and Papuanone from Corymbia Dallachiana. *J. Nat. Prod.* **1999**, *62* (3), 487–489. https://doi.org/10.1021/np980350n.

(26) Zhang, X.; Li, Z. C.; Xu, N.; Li, K. B.; Lin, S.; Lu, F. Z.; Du, F. S.; Li, F. M. β-Diketones Bearing Electron-Donating Chromophores and a Novel β-Triketone: Synthesis and

Reversible Fluorescence Behavior. *Tetrahedron Lett*. **2006**, *47* (15), 2623–2626. https://doi.org/10.1016/j.tetlet.2006.02.019.

(27) Zou, Y.; Gong, S.; Xie, G.; Yang, C. Design Strategy for Solution-Processable Thermally Activated Delayed Fluorescence Emitters and Their Applications in Organic Light-Emitting Diodes. *Adv. Opt. Mater*. **2018**, *6* (23), 1–25. https://doi.org/10.1002/adom.201800568.

(28) Huang, T.; Jiang, W.; Duan, L. Recent Progress in Solution Processable TADF Materials for Organic Light-Emitting Diodes. *J. Mater. Chem. C* **2018**, *6* (21), 5577–5596. https://doi.org/10.1039/c8tc01139g.

(29) Reid, B. L.; Stagni, S.; Malicka, J. M.; Cocchi, M.; Hanan, G. S.; Ogden, M. I.; Massi, M. Lanthanoid β-Triketonates: A New Class of Highly Efficient NIR Emitters for Bright NIR-OLEDs. *Chem. Commun*. **2014**, *50* (78), 11580–11582. https://doi.org/10.1039/c4cc04961f.

(30) Bai, M.-D.; Zhang, M.; Wang, K.; Shi, Y.-Z.; Chen, J.-X.; Lin, H.; Tao, S.-L.; Zheng, C.-J.; Zhang, X.-H. Novel Star-Shaped Yellow Thermally Activated Delayed Fluorescence Emitter Realizing over 10% External Quantum Efficiency at High Luminance of 30000 Cd M−2 in OLED. *Org. Electron*. **2018**, *62* (August), 220–226. https://doi.org/10.1016/j.orgel.2018.08.021.

(31) Hansen, P. E.; Spanget-Larsen, J. NMR and IR Investigations of Strong Intramolecular Hydrogen Bonds. *Molecules* **2017**, *22* (4). https://doi.org/10.3390/molecules22040552.

(32) Charisiadis, P.; Kontogianni, V. G.; Tsiafoulis, C. G.; Tzakos, A. G.; Siskos, M.; Gerothanassis, I. P. 1H-NMR as a Structural and Analytical Tool of Intra- and

Intermolecular Hydrogen Bonds of Phenol-Containing Natural Products and Model Compounds. *Molecules* **2014**, *19* (9), 13643–13682. https://doi.org/10.3390/molecules190913643.

(33) Yoshimi, Y.; Maeda, H.; Hatanaka, M.; Mizuno, K. Intramolecular 9-Membered Hydrogen Bonding of 2-Arylmethylphenols Having Carbonyl Groups at 2′-Position. *Tetrahedron* **2004**, *60* (42), 9425–9431. https://doi.org/10.1016/j.tet.2004.08.007.

(34) Connelly, N. G.; Geiger, W. E. Chemical Redox Agents for Organometallic Chemistry. *Chem. Rev.* **1996**, *96* (2), 877–910. https://doi.org/10.1021/cr940053x.

(35) Cardona, C. M.; Li, W.; Kaifer, A. E.; Stockdale, D.; Bazan, G. C. Electrochemical Considerations for Determining Absolute Frontier Orbital Energy Levels of Conjugated Polymers for Solar Cell Applications. *Adv. Mater.* **2011**, *23* (20), 2367–2371. https://doi.org/10.1002/adma.201004554.

(36) Brouwer, A. M. Standards for Photoluminescence Quantum Yield Measurements in Solution (IUPAC Technical Report). *Pure Appl. Chem.* **2011**, *83* (12), 2213–2228. https://doi.org/10.1351/PAC-REP-10-09-31.

(37) Nakamaru, K. RuBPY Lifetime Nakamaru 890 Ns in N2 Bubbled MeCN.Pdf. *Bull. Chem. Soc. Jpn.* 1982, pp 2697–2705.

(38) Baraket, F.; Pedras, B.; Torres, É.; Brites, M. J.; Dammak, M.; Berberan-Santos, M. N. Novel Phenoxazine-Benzonitrile and Phenothiazine-Benzonitrile Donor-Acceptor Molecules with Thermally Activated Delayed Fluorescence (TADF). *Dye. Pigment.* **2020**, *175* (October 2019), 1–5. https://doi.org/10.1016/j.dyepig.2019.108114.

(39) Prommin, C.; Kanlayakan, N.; Chansen, W.; Salaeh, R.; Kerdpol, K.; Daengngern, R.; Kungwan, N. Theoretical Insights on Solvent Control of Intramolecular and Intermolecular Proton Transfer of 2-(2′-Hydroxyphenyl)Benzimidazole. *J. Phys. Chem. A* **2017**, *121* (31), 5773–5784. https://doi.org/10.1021/acs.jpca.7b03454.

(40) Nakanotani, H.; Higuchi, T.; Furukawa, T.; Masui, K.; Morimoto, K.; Numata, M.; Tanaka, H.; Sagara, Y.; Yasuda, T.; Adachi, C. High-Efficiency Organic Light-Emitting Diodes with Fluorescent Emitters. *Nat. Commun.* **2014**, *5* (May), 1–7. https://doi.org/10.1038/ncomms5016.

(41) Mohanty, J.; Nau, W. M. Refractive Index Effects on the Oscillator Strength and Radiative Decay Rate of 2{,}3-Diazabicyclo[2.2.2]Oct-2-Ene. *Photochem. Photobiol. Sci* **2004**, *3*, 1026– 1031.

(42) dos Santos, P. L.; Ward, J. S.; Congrave, D. G.; Batsanov, A. S.; Eng, J.; Stacey, J. E.; Penfold, T. J.; Monkman, A. P.; Bryce, M. R. Triazatruxene: A Rigid Central Donor Unit for a D–A3 Thermally Activated Delayed Fluorescence Material Exhibiting Sub-Microsecond Reverse Intersystem Crossing and Unity Quantum Yield via Multiple Singlet–Triplet State Pairs. *Adv. Sci.* **2018**, *5* (6), 1–9. https://doi.org/10.1002/advs.201700989.

(43) Wang, H.; Xie, L.; Peng, Q.; Meng, L.; Wang, Y.; Yi, Y.; Wang, P. Novel Thermally Activated Delayed Fluorescence Materials-Thioxanthone Derivatives and Their Applications for Highly Efficient OLEDs. *Adv. Mater.* **2014**, *26* (30), 5198–5204. https://doi.org/10.1002/adma.201401393.

(44) Tanaka, H.; Shizu, K.; Nakanotani, H.; Adachi, C. Twisted Intramolecular Charge Transfer

State for Long-Wavelength Thermally Activated Delayed Fluorescence. *Chem. Mater.* **2013**, *25* (18), 3766–3771. https://doi.org/10.1021/cm402428a.

(45) Hirata, S.; Sakai, Y.; Masui, K.; Tanaka, H.; Lee, S. Y.; Nomura, H.; Nakamura, N.; Yasumatsu, M.; Nakanotani, H.; Zhang, Q.; Shizu, K.; Miyazaki, H.; Adachi, C. Highly Efficient Blue Electroluminescence Based on Thermally Activated Delayed Fluorescence. *Nat. Mater.* **2015**, *14* (3), 330–336. https://doi.org/10.1038/nmat4154.

(46) Su, S. J.; Chiba, T.; Takeda, T.; Kido, J. Pyridine-Containing Triphenylbenzene Derivatives with High Electron Mobility for Highly Efficient Phosphorescent OLEDs. *Adv. Mater.* **2008**, *20* (11), 2125–2130. https://doi.org/10.1002/adma.200701730.

(47) Zeng, W.; Lai, H. Y.; Lee, W. K.; Jiao, M.; Shiu, Y. J.; Zhong, C.; Gong, S.; Zhou, T.; Xie, G.; Sarma, M.; Wong, K. T.; Wu, C. C.; Yang, C. Achieving Nearly 30% External Quantum Efficiency for Orange–Red Organic Light Emitting Diodes by Employing Thermally Activated Delayed Fluorescence Emitters Composed of 1,8-Naphthalimide-Acridine Hybrids. *Adv. Mater.* **2018**, *30* (5), 1–8. https://doi.org/10.1002/adma.201704961.

(48) Xie, G.; Li, X.; Chen, D.; Wang, Z.; Cai, X.; Chen, D.; Li, Y.; Liu, K.; Cao, Y.; Su, S. J. Evaporation- and Solution-Process-Feasible Highly Efficient Thianthrene-9,9′,10,10′-Tetraoxide-Based Thermally Activated Delayed Fluorescence Emitters with Reduced Efficiency Roll-Off. *Adv. Mater.* **2016**, *28* (1), 181–187. https://doi.org/10.1002/adma.201503225.

(49) Song, F.; Wei, G.; Jiang, X.; Li, F.; Zhu, C.; Cheng, Y. Chiral Sensing for Induced Circularly Polarized Luminescence Using an Eu()-Containing Polymer and D- or L-Proline.

Chem. Commun. **2013**, *49* (51), 5772–5774. https://doi.org/10.1039/c3cc42323a.

(50) Frisch G. W.; Schlegel, H. B.; Scuseria, G. E.; Robb, M. A.; Cheeseman, J. R.; Scalmani, G.; Barone, V.; Petersson, G. A.; Nakatsuji, H.; Li, X.; Caricato, M.; Marenich, A. V.; Bloino, J.; Janesko, B. G.; Gomperts, R.; Mennucci, B.; Hratch, D. J., M. J. . T. Gaussian 16, Rev. A.03. *Gaussian, Inc., Wallingford, CT* **2016**. https://doi.org/111.

(51) Adamo, C.; Scuseria, G. E.; Barone, V. Accurate Excitation Energies from Time-Dependent Density Functional Theory: Assessing the PBE0 Model. *J. Chem. Phys.* **1999**, *111* (7), 2889–2899. https://doi.org/10.1063/1.479571.

(52) Tomasi, J.; Mennucci, B.; Cammi, R. Quantum Mechanical Continuum Solvation Models. *Chem. Rev.* **2005**, *105* (8), 2999–3093. https://doi.org/10.1021/cr9904009.

(53) Greenham, N. C.; Samuel, I. D. W.; Hayes, G. R.; Phillips, R. T.; Kessener, Y. A. R. R.; Moratti, S. C.; Holmes, A. B.; Friend, R. H. Measurement of Absolute Photoluminescence Quantum Efficiencies in Conjugated Polymers. *Chem. Phys. Lett.* **1995**, *241* (1–2), 89–96. https://doi.org/10.1016/0009-2614(95)00584-Q.

(54) Masui, K.; Nakanotani, H.; Adachi, C. Analysis of Exciton Annihilation in High-Efficiency Sky-Blue Organic Light-Emitting Diodes with Thermally Activated Delayed Fluorescence. *Org. Electron.* **2013**, *14* (11), 2721–2726. https://doi.org/10.1016/j.orgel.2013.07.010.

Table of Contents: